# The structural origins of brittle star arm kinematics: An integrated tomographic, additive manufacturing, and parametric modeling-based approach

Lara Tomholt[a,b], Larry J. Friesen[c], Daniel Berdichevsky[a,b], Matheus C. Fernandes[a,d], Christoph Pierre[e], Robert J. Wood[a,d], James C. Weaver[a,*]

[a] *Wyss Institute for Biologically Inspired Engineering, Harvard University, 60 Oxford Street, Cambridge, MA 02138, USA*
[b] *Harvard University Graduate School of Design, 48 Quincy St, Cambridge, MA 02138, USA*
[c] *Department of Biological Sciences, Santa Barbara City College, Santa Barbara, CA 93109, USA*
[d] *John A. Paulson School of Engineering and Applied Sciences, Harvard University, Cambridge, MA 02138 USA*
[e] *UCSB Marine Operations, University of California, Santa Barbara, CA 93106, USA*

## ARTICLE INFO

## ABSTRACT

Brittle stars are known for the high flexibility of their arms, a characteristic required for locomotion, food grasping, and for holding onto a great diversity of substrates. Their high agility is facilitated by the numerous discrete skeletal elements (ossicles) running through the center of each arm and embedded in the skin. While much has been learned regarding the structural diversity of these ossicles, which are important characters for taxonomic purposes, their impact on the arms' range of motion, by contrast, is poorly understood. In the present study, we set out to investigate how ossicle morphology and skeletal organization affect the flexibility of brittle star arms.

Here, we present the results of an in-depth analysis of three brittle star species (*Ophioplocus esmarki*, *Ophiopteris papillosa*, and *Ophiothrix spiculata*), chosen for their different ranges of motion, as well as spine size and orientation. Using an integrated approach that combines behavioral studies with parametric modeling, additive manufacturing, micro-computed tomography, scanning electron microscopy, and finite element simulations, we present a high-throughput workflow that provides a fundamental understanding of 3D structure-kinematic relationships in brittle star skeletal systems.

## 1. Introduction

Brittle stars (phylum Echinodermata, class Ophiuroidea) are close relatives of sea stars, and are the most speciose group of modern echinoderms, encompassing more than 2000 species (Meglitsch and Schram, 1991; Stöhr et al., 2018, 2012). They are globally distributed in marine environments and are important contributors to both shallow and deep benthic communities (Stöhr et al., 2012), but are most abundant in shallow tropical and subtropical seas (Austin and Hadfield, 1980).

Brittle stars are known for their long, slender, and highly flexible arms (Barnes, 1987; Stöhr et al., 2012), as described by J. G. Wood in 1898, who so eloquently wrote, "The whole of the brittle stars are curious and restless beings. They can never remain in the same attitude for the tenth part of a second, but are constantly twisting their long arms, as if they were indeed the serpents with which Medusa's head was surrounded."

Due to their lack of cephalization, the terminology used to describe a brittle star's body axis is defined by the location of the mouth, which is located in the middle of the central disk and faces the substrate, thus defining the "oral" and "aboral" (Hyman, 1940; Meglitsch and Schram, 1991) surfaces (or alternatively "ventral" and "dorsal" (Austin and Hadfield, 1980), respectively).

With a central disk ranging from 3 to 50 mm in diameter, their arm lengths vary from ca. two-times their disk diameter to twenty-times or more in some species (Stöhr et al., 2012). The five arms are symmetrically arranged in a pentaradial fashion around the central disk, and they can bend both in-plane (or "laterally" (LeClair and LaBarbara, 1997), perpendicular to the oral-aboral axis) and out-of-plane (or "vertically" (Barnes, 1987; LeClair and LaBarbara, 1997), parallel to the
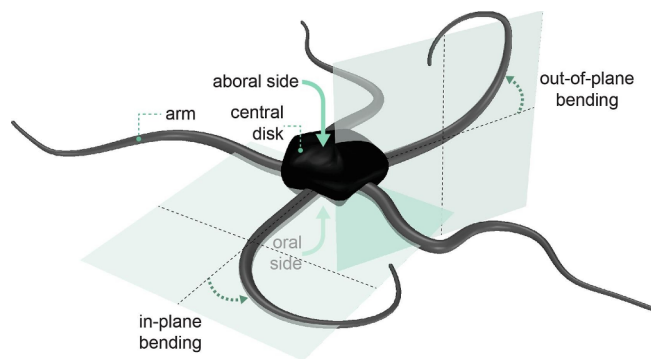
**Fig. 1.** Brittle star external anatomy. Brittle star anatomical descriptions are based on the location of the mouth, which is located in the middle of the central disk, and faces the substrate, and thus defines the oral and aboral surfaces. The five arms, arranged pentaradially around the central disk, can bend both in-plane (perpendicular to the oral-aboral axis) and out-of-plane (parallel to the oral-aboral axis).

oral-aboral axis) (Fig. 1).

As a group, brittle stars are considered to be the most mobile echinoderms (Barnes, 1987). Arm movements play a major role in their unique mode of locomotion since, unlike sea stars, most brittle stars do not use their tube feet for this purpose (Lawrence, 1987; Romanes, 1893). The muscular limbs apply forces to the substrate, pushing or pulling the body forward across the sea floor. A decentralized nervous system (Cobb and Stubbs, 1981) coordinates repetitive sinusoidal in-plane movements, often in four of the arms, while one leading arm points in the direction of locomotion (Arshavskii et al., 1975; Glaser, 1907; Romanes, 1893; Smith, 1965). The gait patterns observed in most species show no arm preference or an indication of directional polarity, and as such, brittle stars can quickly change direction (Arshavskii et al., 1976; Astley, 2012; Barnes, 1987; Kano et al., 2017; Watanabe et al., 2012).

In addition to locomotion, brittle stars use their arms to hold onto substrates, coiling their flexible arms tightly around structurally complex objects such as kelp, sponges, or corals (Austin and Hadfield, 1980; Lawrence, 1987; Mosher and Watling, 2009), with spines located along the arms aiding in the anchoring process (Austin and Hadfield, 1980). In strong currents, brittle stars have also been observed to interlock arms between adjacent individuals to form stable aggregations (Warner and Woodley, 1975). Arm movements also play a key part in the process of burying themselves in mud or the crevices of rocks (Barnes, 1987; Stöhr et al., 2012). When hiding in small openings, for example, the animals coil their arms, resulting in the formation of robust anchoring postures (LeClair and LaBarbara, 1997).

The arms of brittle stars also operate as feeding structures (Lawrence, 1987; Warner and Woodley, 1975), with both the tube feet and spines playing important roles in the detection of chemical stimuli during feeding (Pentreath, 1970; Sloan and Campbell, 1982). While holding on to the substrate with one or two arms, suspension-feeding species such as the long-armed *Ophiothrix spp.*, for example, extend the remaining arms above the disk and expose them to the prevailing currents, capturing small passing particles with their spines and tube feet, which are then transferred to the mouth (Austin and Hadfield, 1980; Barnes, 1987; Lawrence, 1987; Warner, 1982; Warner and Woodley, 1975). In species such as *Ophiopteris papillosa,* which exhibit more targeted feeding behaviors, the arm spines are used to break off small pieces from larger food items (Austin and Hadfield, 1980), while carnivorous species can actively grab large prey items directly through rapid arm coiling, and carry them to the mouth (Barnes, 1987; Hyman, 1940; Lawrence, 1987; Warner, 1982; Warner and Woodley, 1975).

Brittle stars and other echinoderms possess a dermal endoskeleton consisting of numerous small porous calcareous skeletal elements (ossicles), which exhibit a wide range of species-specific geometries (Stöhr

et al., 2012). Their positions are maintained by connective tissues (Bray, 1985), and the interaction between the arms' internal skeleton, the muscles, and soft connective tissues allows for a large number of degrees of freedom during arm bending (Byrne and Hendler, 1988; Lawrence, 1987; LeClair and LaBarbara, 1997). The extent of skeletal development is often associated with a brittle star's overall level of activity, with delicate skeletal elements facilitating more agile motions, while heavily calcified forms exhibit more sluggish behaviors (Lawrence, 1987).

Historically, the structural diversity of brittle star ossicles have primarily been used for taxonomic purposes (LeClair, 1996; Lyman, 1882; O'Hara et al., 2014; Smith et al., 1995; Stöhr et al., 2012; Thuy and Stöhr, 2011), and the species-specific spiny ornamentations on the arms are thought to be closely tied to the structural complexity of the habitats in which each species is found (Austin and Hadfield, 1980; Hendler and Miller, 1984). Hard substrate dominated rocky reefs are commonly home to the smooth-armed and heavily armored brittle stars, whereas spiny brittle stars frequently live in more structurally complex or soft substrate-dominated communities (Fig. 2).

Brittle star studies from the past few decades have primarily focused on arm regeneration and the formation of the calcitic skeleton (Carnevali, 2006; Czarkwiani et al., 2016, 2013; Skold and Rosenberg, 1996; Zeleny, 1903), nervous system structural complexity (Cobb and Stubbs, 1981), and the relationships between neurophysiology, arm movement, and locomotion (Astley, 2012; Glaser, 1907; Kano et al., 2017; Moore and Cobb, 1986; Watanabe et al., 2012). From a historical perspective, while much has been learned regarding ossicle structural diversity (Lyman, 1882), their impact on the arms' range of motion is still poorly understood (Thuy and Stöhr, 2011).

Inspired by their impressive flexibility, we set out to develop an integrated approach to identify how ossicle morphology and skeletal organization dictate the kinematics of brittle star arms, a study that builds on recent advances in this field (Clark et al., 2018). Here, we present the results of an in-depth analysis of three brittle star species, purposely chosen for their distinctive level of agility and extent of skeletal development. By combining behavioral studies with parametric modeling, additive manufacturing, micro-computed tomography, scanning electron microscopy, and finite element simulations, we present a high-throughput workflow that provides critical kinematic insights into structure-function relationships in brittle star skeletal systems.

## 2. Methods and materials

### 2.1. Research species

We selected three anatomically distinct species of brittle stars from the temperate North Eastern Pacific for the purpose of this study: *Ophioplocus esmarki*, *Ophiopteris papillosa*, and *Ophiothrix spiculata* (Fig. 3). While these three species belong to different brittle star families, they can grow to similar sizes, making detailed comparative anatomical studies between them relatively straightforward. These species also vary in their degree of agility, extent of skeletal armament, the relative size and morphology of their arm spines, and how they employ their arms for feeding. For example, *O. esmarki* feeds on small animals, while *O. spiculata* is primarily a suspension feeder, and *O. papillosa* is both a suspension feeder as well as an active carnivore (Austin and Hadfield, 1980).

*O. esmarki* can be found from the lower rocky intertidal to depths of 70 m, and is a relatively inactive species, with stiff and relatively short arms (two to three times as long as its central disk diameter), with very few and very small spines that are capable of being folded against the arms (Austin and Hadfield, 1980). In contrast, both *O. papillosa* and *O. spiculata* are often seen in algal holdfasts and other sheltered habitats, from the lower intertidal to depths greater than 100 m, and have relatively longer and more agile arms, as well as longer and more

**Fig. 2.** Habitat preference in smooth and spiny brittle star species. Rocky reef habitats (A) are common homes to smooth-armed brittle stars (B) that hide under rocks or in crevices and are protected by their robust dermal armament (cf. Fig. 4). In contrast, soft substrate-dominated habitats such as kelp forests (C) are common homes for spiny brittle stars (D) where their high aspect ratio spines can aid in successfully grasping onto structurally complex substrates for protection.



*Ophioplocus esmarki* ⊓ 1 cm      *Ophiopteris papillosa* ⊓ 1 cm      *Ophiothrix spiculata* ⊓ 1 cm

**Fig. 3.** Aboral views of the three brittle star species used in the present study. The arms of *O. esmarki* are relatively thick with small, stubby spines, whereas the arms of *O. papillosa* and *O. spiculata* exhibit longer, higher aspect ratio spines attached to comparatively thinner arms. The spines of *O. papillosa* are arranged in a highly parallel fashion, while the spines of *O. spiculata* exhibit a more disordered organization.

numerous spines than *O. esmarki*. The relatively smooth arm spines of *O. papillosa* are blunt and flattened and exhibit a highly parallel ordering along each side of the arm, while the spines of *O. spiculata* point in seemingly random directions and exhibit well-defined surface barbs (Austin and Hadfield, 1980).

### 2.2. Specimen collection and housing

All three species were collected off the coast of Santa Barbara, California at depths of 10–15 m, ranged between 10 and 20 cm in total specimen diameter, and, for the selected specimens described here, were chosen such that they did not exhibit significant recent arm regeneration. Live individuals were maintained in a temperate flow-through seawater system at ca. 15 °C and placed in small black-bottom aquaria for photographic and behavioral studies (Figs. 8–10). For all of the behavior and anatomical studies described in the following sections,

and unless directly specified, at least 10 individuals of each species were investigated and the results reported here for the selected individuals are representative of the trends observed.

### 2.3. Live specimen photography

Live brittle stars were transferred from seawater holding tanks to photography trays with black sides and black velvet bottoms and placed on a 3 mm thick glass sheet, supported 2 cm below the seawater surface and 7 cm above the velvet bottom. Images were captured using a Canon EOS 7D Mark II with a Canon EF-S 60 mm f/2.8 Macro USM lens with settings of ISO 100, f/14, and 1/250 s. A single, hand-held electronic strobe (Altura Speedlight AP-FLS-UNV1), triggered by way of a wireless transmitter-receiver pair (Phottix Strato ll Multi 5-in-1 Wireless Trigger System) supplied illumination.
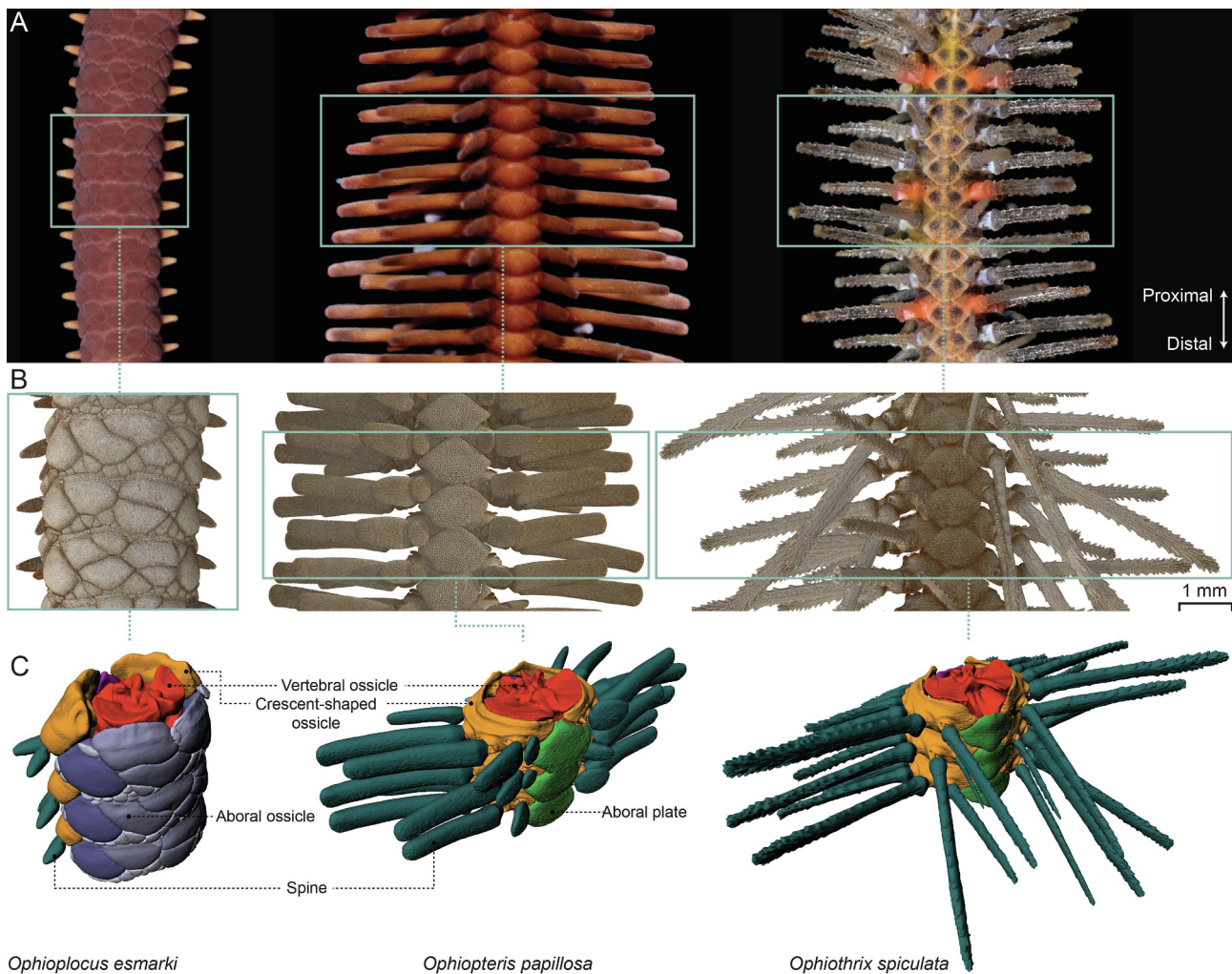
**Fig. 4.** Sequential data processing workflow for identification of the constituent ossicles from three brittle star species. A. Photographs of aboral mid-arm regions and B. their corresponding volume renderings from reconstructed micro-CT data. C. The chain of vertebral ossicles (red) running through the center of each arm is flanked by a series of crescent-shaped ossicles (yellow). Vertebral ossicles of *O. papillosa* and *O. spiculata* are further covered with a series of overlapping aboral plates (light green), while the aboral sides of the arms of *O. esmarki* are covered in a compact voronoi-like fractal arrangement of smaller ossicles (shown in light, medium, and dark purple). The highly mobile spines (dark blue-green) articulate to the crescent-shaped ossicles in a ball-and-socket-like fashion. (For interpretation of the references to color in this figure legend, the reader is referred to the web version of this article.)

### 2.4. Large-scale micro-computed tomography

Micro-computed tomography (micro-CT) studies were performed with 70% ethanol-preserved individuals that were collected from the same localities described above. Specimens were either scanned in their entirety (Fig. 8), or were subdivided into smaller sections for more detailed analyses (Figs. 4 and 5). Using this approach, we were able to virtually remove soft tissues from the specimens (through selective digital filtering of the raw tomography data) and extract information on the size, quantity, and organization of the ossicles within the arms for each species. In addition, this technique permitted the identification of internal and external porosity gradients within each ossicle type, which may play important roles in providing abrasion resistance during arm motion.

Whole (intact) brittle stars (Fig. 8) or isolated ethanol-preserved mid-sections of the arms of all three species, measuring roughly 3 cm in length (Figs. 4 and 5), were stabilized between pieces of soft foam in a plastic tube and scanned with an X-Tek HMXST225 (X-Tek, Amherst, NH, USA) micro-CT x-ray imaging system. The scan resolutions ranged between voxel sizes of 5.035 and 6.889 μm, volumetric reconstructions were generated using VGStudio Max 3.0 (Volume Graphics, Heidelberg, Germany) (Fig. 4B and 5A), and their corresponding data image stacks were exported for further use.

### 2.5. Small-scale micro-computed tomography

In order to examine the surface and subsurface porosity gradients at identified areas of ossicle-ossicle contact (which may play important roles in providing abrasion resistance during arm motion), we used a SkyScan 2214 micro-CT scanner (Bruker, Billerica, USA) with a pixel resolution of 0.680 μm to acquire a high resolution volumetric reconstruction from a representative vertebral ossicle, measuring ca. 2 mm in diameter, obtained from the mid-region of an arm from *O. papillosa*. The generated 3D surface model (see details in Section 2.6) was then imported into Rhinoceros 6.0 (Robert McNeel & Associates, Seattle, WA, USA) and used for visualization and animation purposes (Fig. 15A).
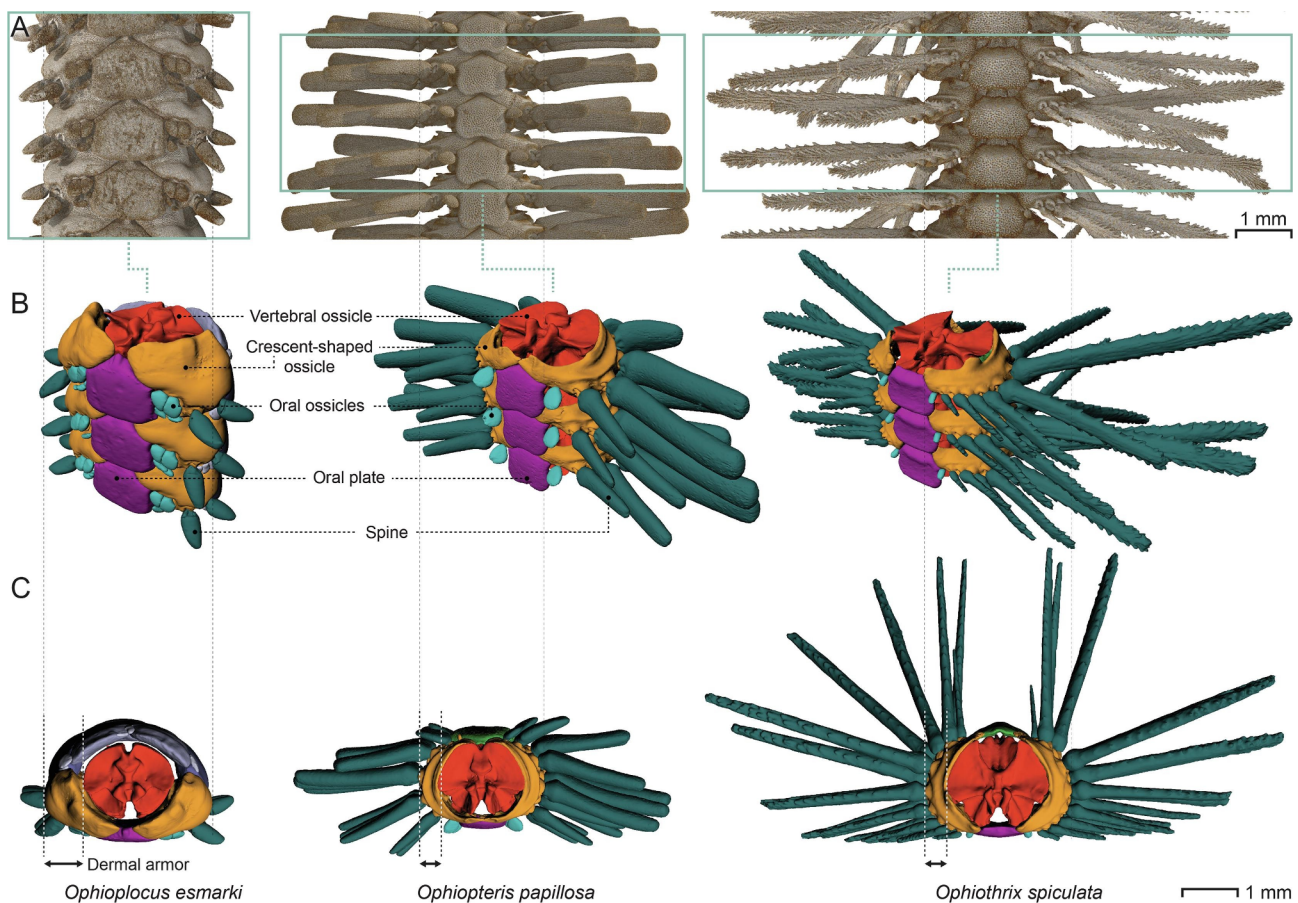
**Fig. 5.** Structural characterization of oral ossicles from the arms of three brittle star species. A. Volume rendering of reconstructed micro-CT data, showing the arm segments from the oral side. B. In this orientation, the crescent-shaped ossicles (yellow), oral plates (magenta) and small oral ossicles (light blue) are clearly visible. In contrast to the aboral ossicles (cf. Fig. 4), the oral plates (magenta) covering the vertebral ossicles (red) are structurally similar and vary only slightly in size and shape between the three species. C. Proximal-distal views of the three ossicle groups showing differences in number and size of spines (dark blue-green) between species, as well as the thickness of the dermal armor, which is appreciably thicker in *O. esmarki*. (For interpretation of the references to color in this figure legend, the reader is referred to the web version of this article.)

### 2.6. Data segmentation

Since individual ossicle geometries and overall skeletal organization patterns are challenging to distinguish in grayscale intensity-based volume renderings, we used Materialise Mimics (Materialise, Leuven, Belgium), a medical image processing software, to segment out individual ossicles and obtain clear depictions of their morphologies. The micro-CT z-image stacks were imported into the software, specifying the image pixel size to maintain the original arm dimensions. Using selected thresholding of grayscale intensity values and region-growing, a mask of the electron dense ossicle structure was created. Subsequently, manual slice-by-slice editing, region growing, and boolean operations were employed to separate the ossicles into individual masks. Finally, a 3D surface reconstruction was performed from each ossicle mask, which in turn were exported in stereolithography (STL) file formats for further processing.

### 2.7. 3D printing

The virtual three-dimensional models constructed from the micro-CT and segmentation-based workflow revealed a great deal of information regarding ossicle geometry and ultrastructure, but in order to gain insight into their functionality in arm kinematics, we next employed a combination of additive manufacturing (3D printing) and parametric modeling approaches.

3D printing provides a highly complementary approach to traditional digital renderings in that tangible models have the advantage of quickly being able to identify mechanical interferences in complex linkage systems (Clark et al., 2019). To prepare the models for 3D printing, the ossicle STL files were imported into Rhinoceros 6.0 for additional post processing, which included surface smoothing and the removal of interior voids. The ossicles were then manually classified into seven color-coded ossicle types (Figs. 4 and 5) and 3D printed. Each ossicle group (or "metameric unit" (Czarkwiani et al., 2016)) (Fig. 6, upper images) was printed at 20 times its original size on a Stratasys J750 (Stratasys, Eden Prairie, MN, USA) multi-material color 3D printer. This specific 3D printer was chosen to obtain physical models illustrating the various ossicle types with different colors, and for its printing technique which employs an easily removable support material (Fig. 6).

For the kinematic studies, we employed the use of a Connex500 (Stratasys, Eden Prairie, USA) multi-material 3D printer. For each ossicle group, the vertebral ossicles were printed from a rigid material (Young's modulus, ca. 1 GPa), while the flanking ossicles were printed from a lower modulus material (Young's modulus, ca. 5 MPa). The small contact areas between adjacent ossicles created a multi-ossicle
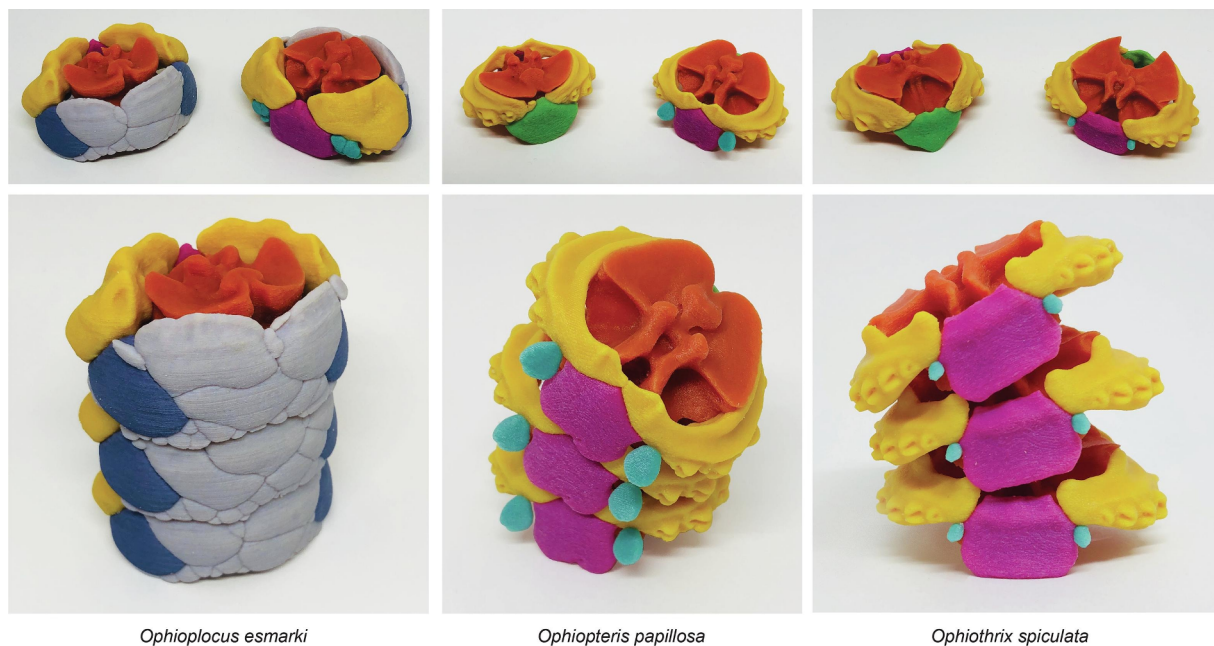
**Fig. 6.** Color-coded 3D-printed models of three adjacent ossicle groups indicating corresponding ossicle types in each brittle star species. The models include the vertebral ossicles (red), crescent-shaped ossicles (yellow), oral plates (magenta), aboral plates in *O. papillosa* and *O. spiculata* (green), aboral ossicles in *O. esmarki* (light gray and dark blue), and oral ossicles (light blue), but exclude the spines. The interactions between the three 3D-printed ossicle groups of *O. papillosa* and *O. spiculata* show a high degree of both in-plane and out-of-plane bending due to their reduced intervertebral dermal armor and large lateral openings, while the organization in *O. esmarki* reveals almost no exposed internal arm regions due dense packing of the fractal-like aboral ossicles. (For interpretation of the references to color in this figure legend, the reader is referred to the web version of this article.)

construct with "living" hinges that allowed us to directly observe regions of contact between adjacent ossicle groups as well as ossicle sliding behavior during arm bending experiments.

### 2.8. Parametric modeling

During the development of our parametric models, several independent data streams were combined to help with their refinement and validation. For example, while the organization of the brittle star arm musculature and associated connective tissues has been described previously (Saita et al., 1982; Stauber and Märkel, 1988; Wilkie, 1978, 2016), it was not known to what extent the preservation of brittle star specimens altered the spacing between adjacent multi-ossicle units or the individual ossicles themselves. Since it was the micro-CT data from the ethanol-preserved specimens that provided the basic geometries and spatial relations from which our kinematic models were constructed, we explored the potential densification of the skeletal system by comparing our ethanol-preserved brittle star micro-CT data (Fig. 4B) to the photos obtained from our live animal behavior studies (Fig. 4A). Since the live animal photos were of high enough resolution to resolve the major ossicle features, they provided robust landmarks for performing such comparisons. These results demonstrated imperceivable (and statistically insignificant) differences between the ossicle spacing in live and ethanol-preserved specimens, confirming the validity of using micro-CT datasets as a basis for the generation of kinematic models.

The kinematic models were created using Rhinoceros 6.0 and its Grasshopper plug-in (Robert McNeel & Associates, Seattle, WA, USA), which is a visual programming language that allows for parametric modeling of complex 3D geometries (Frølich et al., 2017). The software was first used to analyze arm curvatures from a 3D model of a CT-scanned complete brittle star (Fig. 8) and from plan-view photos taken during behavioral studies (Fig. 9). Three dimensional curves were drawn through the central axis of each arm and through the aboral

plates (the latter to determine the orientation of the arm and consequently distinguish in-plane and out-of-plane curvatures), the locations of the ossicle groups were mapped onto each central curve as a series of points (with each point representing the proximal face of the vertebral ossicle), and the local curvature at each point was calculated from the two adjacent points.

Parametric modeling also provided critical insight into the specific functions of the distinct ossicle types, the vertebral ossicles' points of rotation, and achievable range of movement. The parametric script we subsequently developed adjusted the position and orientation of the ossicles based on the two major parameter inputs for in-plane and out-of-plane curvature. The script accounted for the complex interaction between ossicles, as observed during the *in vivo* studies, the micro-CT scans, and interactions with the 3D printed models, by changing the orientation of the ossicle groups during arm bending. The script also accommodated small amounts of in-plane sliding (by a moving point of rotation relative to the interacting ossicle groups), allowed for rotation of the oral and aboral plates during out-of-plane movement, and the detection of movement of vertebral and crescent-shaped ossicles and spines upon collision. The point of rotation and maximum range of curvature was derived from mechanical inferences between 3D-printed ossicle groups and close inspection of individual ossicles (from both micro-CT and SEM data), which revealed corresponding local surface morphologies between proximal and distal surfaces of ossicles of the same type or between ossicles of different types due to mechanical interactions. Rendered images and animations of arm bending were subsequently generated using this parametric design workflow (Figs. 10–13, and the Supplemental videos).

### 2.9. Scanning electron microscopy

Excised multi-joint sections of *O. papillosa* arms were dissociated in a solution of 5.25% sodium hypochlorite to isolate the individual ossicles. The disarticulated ossicles were rinsed three times in calcium
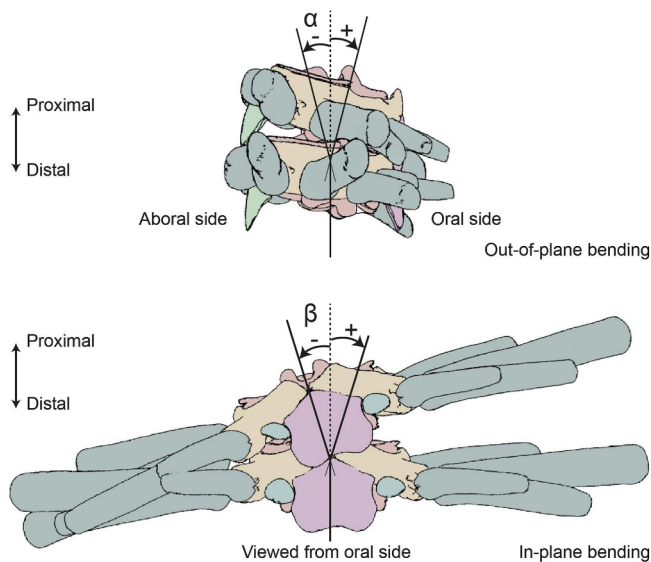
**Fig. 7.** Quantification of arm flexibility. The range of arm curvature represents the angle between the proximal-distal axes through two adjacent vertebral ossicles. The out-of-plane and in-plane bending angles, α and β respectively, can exhibit either positive or negative values, depending on the direction of bending.

carbonate-saturated deionized water, followed by a final rinse in 100% ethanol, and then air dried. The ossicles were mounted to aluminum pin mounts using conductive carbon tape, sputter coated with gold, and imaged with a Tescan (Brno, Czech Republic) Vega3 GMU scanning electron microscope (Fig. 14). These SEM imaging studies allowed us to directly compare the predicted zones of contact between adjacent ossicles during arm bending with local micro-scale variations in skeletal porosity.

### 2.10. Ossicle porosity quantification

Quantitative mapping of the internal architecture of vertebral ossicles (Fig. 15B), based on high-resolution micro-CT data, was performed using DragonflyTM v4.1 software (Object Research Systems Inc., Montréal, Canada). Semi-automated segmentation of the ossicle mineral fraction was based on global grayscale thresholding using Otsu's method (Otsu, 1979). Within the segmented region of interest (ROI), 99.999% of labeled voxels belonged to the continuous calcified skeleton, and the remaining single voxels were discarded from the volume of interest. The thickness mapping operation (Volume Thickness Map) involved the inscription of spheres of the largest radius within the selected ROIs of the skeleton, the results from which were used to generate the color maps shown in Fig. 15B.

### 2.11. Finite element analysis

To investigate the potential functionality of the ossicle stereom porosity gradients observed in the high resolution micro-CT and SEM studies, we performed Finite Element simulations to mimic adjacent ossicle-ossicle collision events during arm bending. The Finite Element model was created using the commercial software ABAQUS 2018 Standard/Explicit (Dassault Systèmes, Johnston, Rhode Island, USA). The geometry of a representative vertebral ossicle, reconstructed from micro-CT data obtained from a central portion of an arm of *O. papillosa*, underwent a series of mesh smoothing operations to create a solid geometry, and was subsequently imported as an IGES file to the simulation software. To effectively define realistic boundary conditions, we

imported a three-part vertebral chain, composed of one vertebral ossicle in its entirety, and one half of an ossicle on each side (Fig. 15C). All three parts of the geometry were defined using a fully solid 3D section with 4-noded linear tetrahedral elements and discretized with a seed size of 0.25 mm, resulting in approximately 40,000 elements in total. The model was generated using an isotropic linear elastic material with a Young's modulus of 72.4 GPa and a Poisson's ratio of 0.3 (as reported for a geological calcite mineral standard). A general hard contact interaction was defined between all nodes of the geometry, neglecting any effects of friction, and displacement boundary conditions were applied to both flat faces of the half-ossicles (Fig. 15C). To accurately obtain the quasi-static solution, we performed this analysis using mass-scaling, ensuring that the model's kinetic energy was at least two orders of magnitude lower than the internal energy of the geometry. The results reported here were acquired from the middle ossicle of the three-part model (where the boundary conditions accurately reflected the interaction between the three ossicles, as illustrated in Fig. 15D-F).

## 3. Results

### 3.1. Micro-CT reconstruction, ossicle segmentation, and additive manufacturing

The 3D reconstructions of the arm segments were used to identify species-specific variability in ossicle morphology (Fig. 4B and 5A), and provided the basis for the generation of the larger-scale kinematic models discussed in the following sections.

In all three species investigated, the central axis of each arm is supported by a series of vertebral ossicles (named for their similarity to chordate spinal vertebrae), which are connected by pairs of muscles, and are responsible for large-scale bending motions. The linear array of vertebral ossicles is further flanked by two parallel rows of crescent-shaped lateral ossicles (or "lateral (arm) plates" as described by Austin and Hadfield, 1980; Thuy and Stöhr, 2011 or "lateral shields" by Hyman, 1940), that bear protuberances to which the highly mobile spines articulate in a ball and socket-like fashion (Wilkie, 2016) (Fig. 4C and 5B). The slender crescent-shaped ossicles of *O. papillosa* and *O. spiculata* are rather similar in shape, while those of *O. esmarki* are shorter and thicker, covering more surface area along the lateral margins of the arms.

The oral faces of the vertebral ossicles are covered by oral plates (or "ventral arm plates" as described by Austin and Hadfield, 1980; Byrne, 1994; Stöhr et al., 2012), which are clearly discernible in the arms of all three species, albeit of slightly different shapes and sizes (Fig. 4). The arms of *O. papillosa* and *O. spiculata* are further covered with a series of aboral plates (or "dorsal arm plates" as described by Austin and Hadfield, 1980; Byrne, 1994; Stöhr et al., 2012), while the aboral surface of the arms of *O. esmarki* are covered with a compact voronoi-like fractal arrangement of smaller aboral ossicles. This mosaic of interpolated elements, which can also be observed in other brittle star species (Austin and Hadfield, 1980; Hyman, 1940), extends over a larger aboral surface area, and the crescent-shaped ossicles therefore exhibit a reduced arc length compared to those seen in the spiny brittle stars. While the proximal edges of the oral and aboral plates are connected to the crescent-shaped ossicles, they still allow for a hinge-like motion (Emson and Wilkie, 1982).

The species-specific dermal armor and spine characteristics are most clearly visible from a proximal–distal view (Fig. 5C). While the vertebral ossicles are roughly the same diameter in each species, the spines are appreciably smaller and fewer in number in *O. esmarki*, and conspicuously longer and more abundant in *O. spiculata*. These analyses also reveal that, for a given species, the spines, while varying in length from the oral to the aboral surface, have similar general shapes and surface features (Hyman, 1940).
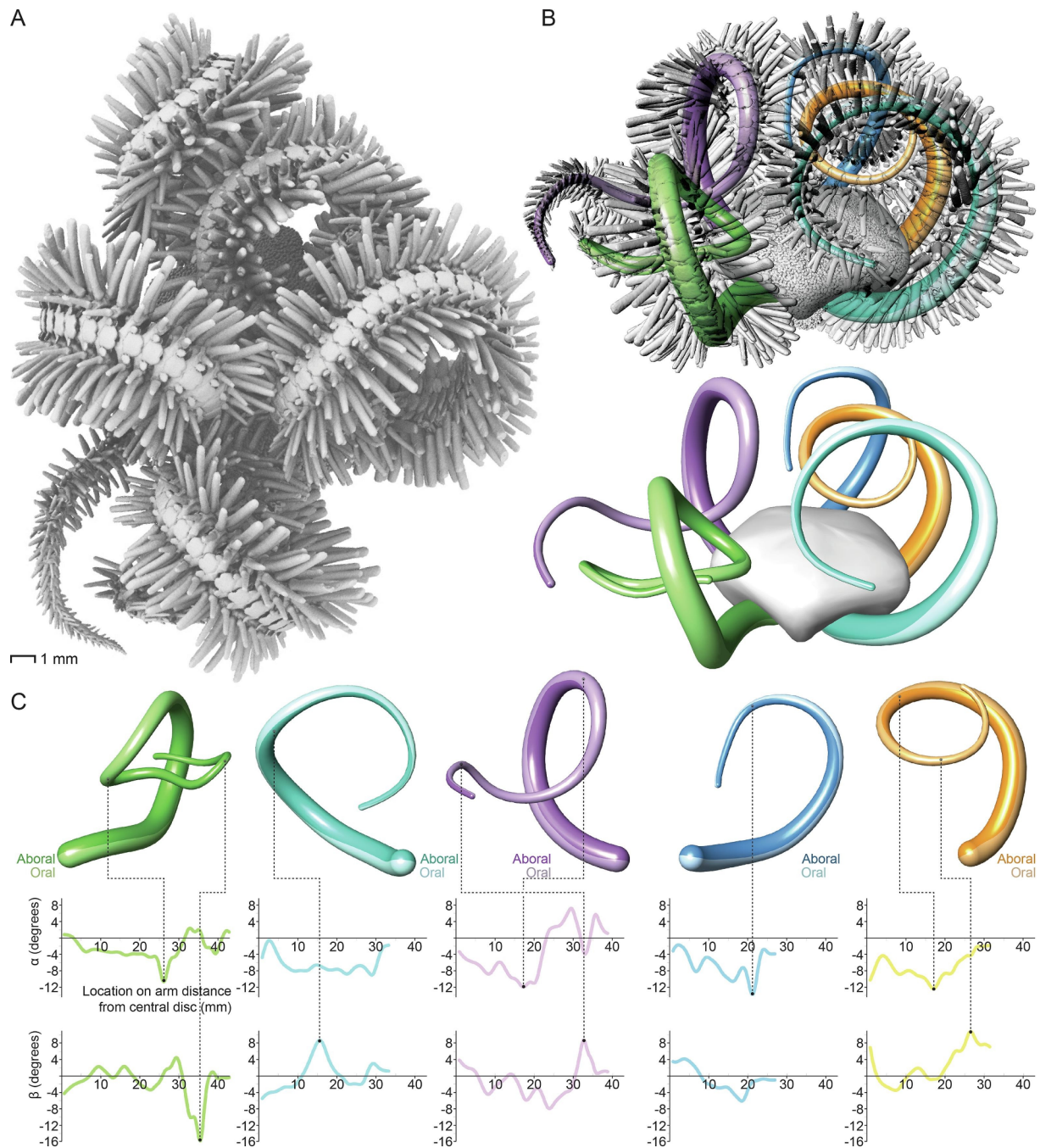
**Fig. 8.** 3D spatial mapping of brittle star arm bending. A. Plan-view rendering (from reconstructed micro-CT data) of the skeletal system of an *O. papillosa* specimen displaying extraordinary out-of-plane arm curling over the central disk. B. The postures of the five arms were traced using our parametric modeling interface. C. Plots of the measured local curvatures show that bending curvature is generally consistent along the length of each arm (α: out-of-plane bending, β: in-plane bending).

While micro-CT data can be very useful for the identification of different ossicle types and their distinctive geometric features, they provide limited information regarding the roles of ossicle geometry in global arm kinematics. In contrast, through the production of tangible physical models via additive manufacturing from the micro-CT source data, we can directly interact with the ossicles in 3D space and thus gain valuable insights into the spatial relationships between adjacent ossicles during large-scale arm motions (Fig. 6).

The vertebral ossicles of the three species articulate in a ball and socket-like fashion, which results from the ossicles' nodes and sockets on the proximal and distal surfaces, also referred to as zygospondylous articulation, and can be found in most brittle stars (Barnes, 1987; Byrne, 1994; Hyman, 1940; Lawrence, 1987; Meglitsch and Schram,

1991; Stöhr et al., 2012). In contrast with a perfect ball and socket articulation possessing a single point of rotation, however, interaction between the 3D printed ossicle groups revealed that some sliding during in-plane and out-of-plane motion was facilitated by the mutually conforming vertebral ossicles' proximal and distal surface morphologies.

Direct physical interactions with the 3D-printed ossicle models of *O. papillosa* and *O. spiculata* clearly demonstrated that maximum in-plane motion is first limited by the collision of adjacent crescent-shaped ossicles, with their proximal and distal geometries corresponding with one another, and mutually jamming at the maximum bending angle. These observations were further supported by micro-CT reconstructions of bent arms from from *O. papillosa* and *O. spiculata,* revealing a comparatively negligible amount of movement of the crescent-shaped
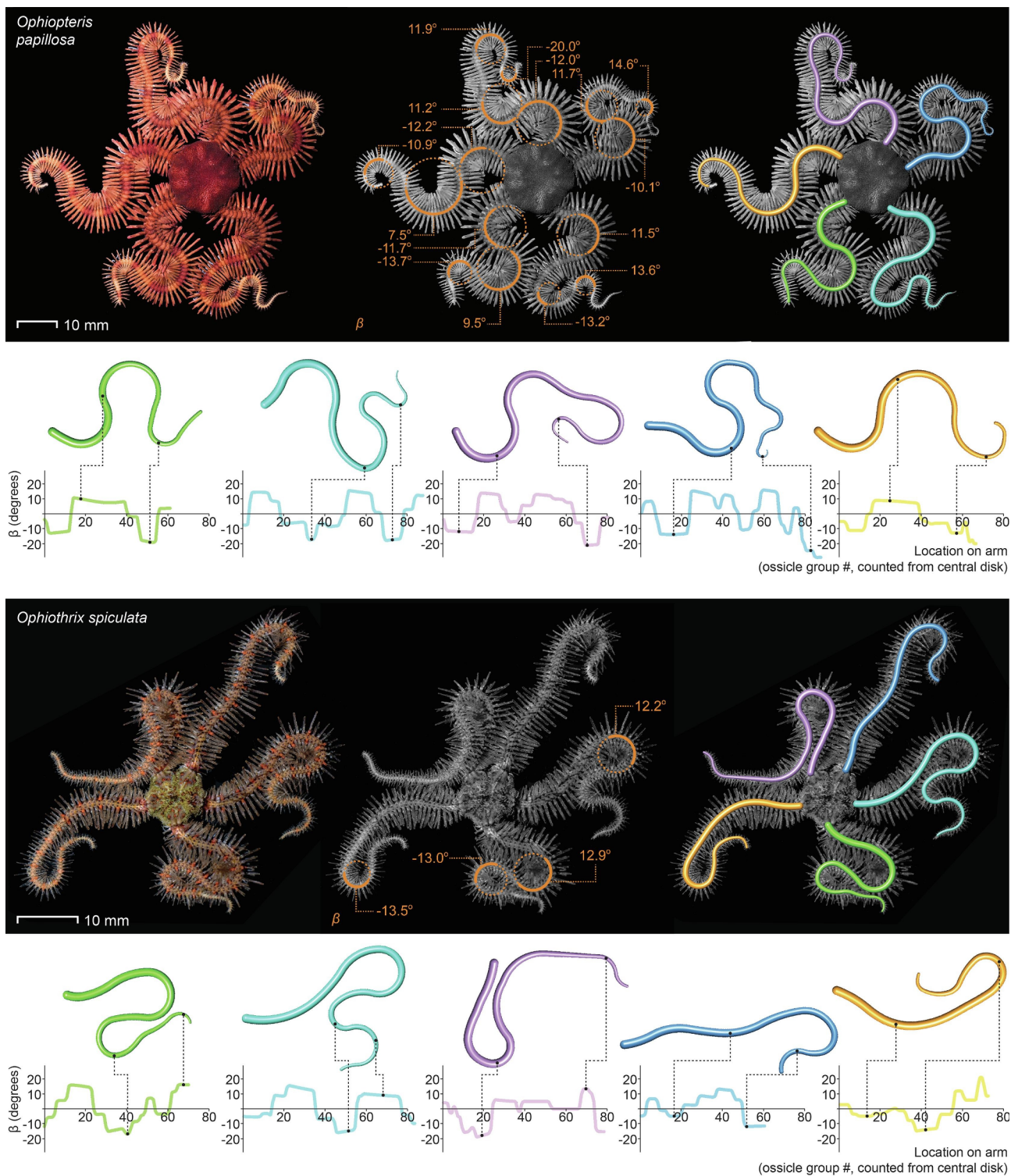
**Fig. 9.** In-plane arm curvature analysis of live brittle star specimens, displaying ranges of arm motion commonly observed in these species. The brittle stars are viewed from their aboral side (in plan-view) and the plots reveal that, except for minor increased curvature near the arm tips, the maximum angle of in-plane curvature (β) remains relatively constant along the length of each arm.

ossicles relative to the vertebral ossicles that they flank. Out-of-plane bending was also possible, but was limited by the oral and aboral plates colliding with adjacent oral and aboral plates and the crescent-shaped ossicles. In contrast, basket stars and some brittle stars that lack aboral arm plates can bend their arms in any direction (Barnes, 1987), which supports the hypothesis of the oral and aboral plates playing a major role in limiting out-of-plane movement (Litvinova, 1994). In addition,

small-scale ossicle features, which were more clearly visible in these enlarged 3D-printed models, provided further evidence for additional out-of-plane bending. For example, the morphology of the oral and aboral plates' interior faces mutually conform to those of their exterior faces as well as to the geometry of ridges located on the crescent-shaped ossicles, illustrating the regions of the oral and aboral plates which slide over one another during out-of-plane bending events.
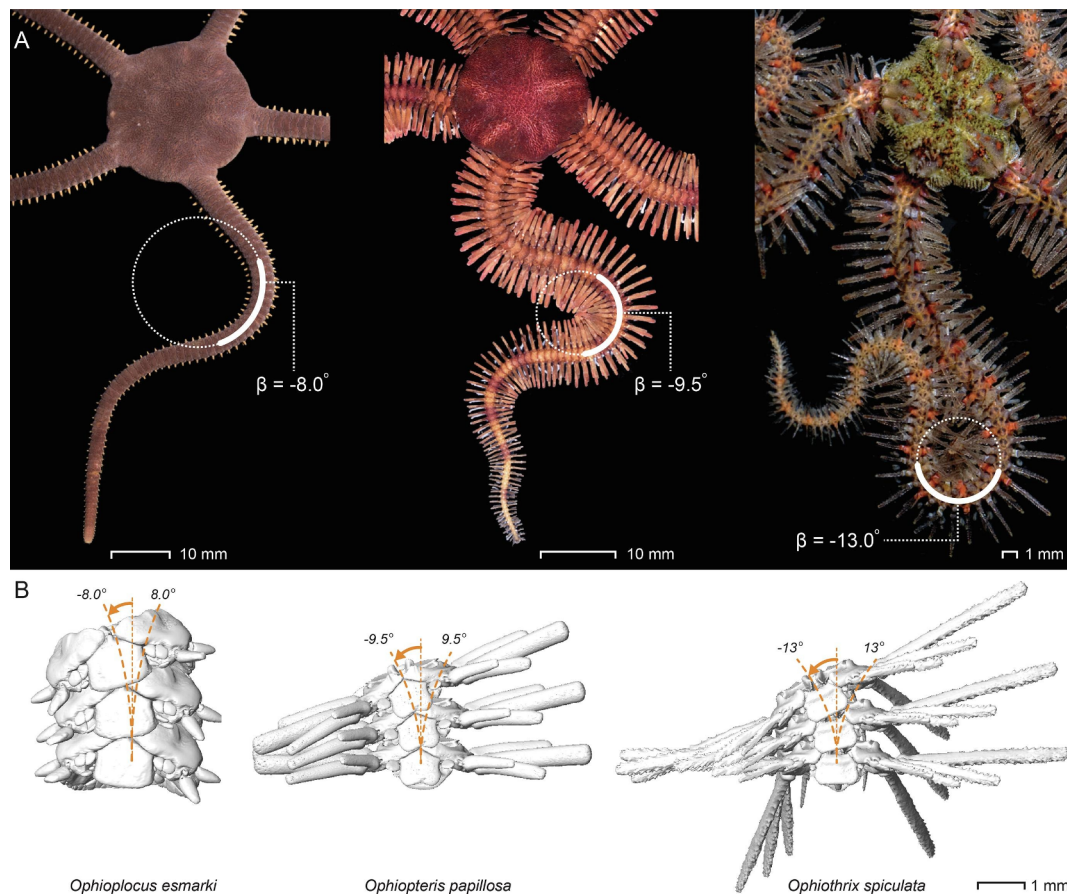
**Fig. 10.** Modeling in-plane bending modes in brittle star arms. A. Maximum in-plane bending observed during behavioral studies, which provided the input for the parametric models of the complete skeletal systems. B. The parametric models show that maximum in-plane bending is limited by the crescent-shaped ossicles (*O. esmarki*) or the spines (*O. papillosa* and *O. spiculata*).

### 3.2. Arm curvature analysis with 3D modeling

The ranges of arm curvature presented in this study represent the angle between the proximal–distal axes through the vertebrae of two adjacent ossicle groups. This metric is independent from specimen size, and therefore allows for an unambiguous comparison between animals of different sizes and different species, as well as from different locations along the length of the arm. The out-of-plane bending angle ($\alpha$) has a positive value for flexion towards the oral side and negative towards the aboral side. The in-plane bending angle ($\beta$) to either side of the arm is also identified by a positive and negative value (Fig. 7).

To better understand the maximum ranges of motion of brittle star arms, whole arm curvature analyses were performed on both live and preserved specimens. The intact preserved specimen of *O. papillosa* that was examined was chosen based on the unique, extremely contorted nature of the arms, which exhibited pronounced in-plane and out-of-plane bending (Fig. 8A), a posture similar to the observed arm coiling behavior described by Emson and Wilkie (1982). For this individual, the postures of the five arms were traced using our parametric modeling interface (Fig. 8B), and the bending angles between adjacent ossicles plotted in separate charts for in-plane and out-of-plane motion (Fig. 8C). The results from these analyses reveal that bending curvature is generally independent along the location on the arm, and thus from ossicle size, although in-plane curvature can reach higher values at the arm tips.

In contrast to the highly contorted arm geometries shown in Fig. 8, during the live-specimen behavioral studies, the brittle stars displayed more typical ranges of arm motion to those observed from numerous *in situ* field studies made previously by the authors (JCW, LJF, and CP, personal observations). Photographs of *O. papillosa and O. spiculata* were subjected to the same method of analysis described above and the measured in-plane bending curvatures showed trends similar to the results plotted in Fig. 8. Apart from slight increases in measured curvature at the arm tips (Clark et al., 2018), which resulted from a decreased size of the ossicle groups towards their distal ends, the measured arm bending angles were generally independent from their location along their length (Fig. 9).

### 3.3. Parametric modeling of arm curvatures

The combined knowledge obtained from interacting with the 3D-printed ossicle groups (Section 3.1) and ranges of arm bending observed in the behavioral studies (Section 3.2) was used for the development of our parametric script. Relevant parameters included the moving center point of rotation, the crescent-shaped and vertebral ossicle morphologies (which dictated limitations of in-plane and out-of-plane bending, respectively), and the maximum bending angles observed during the *in vivo* studies.

The parametric models were developed to identify the relative motions of the ossicles and spines that enabled arm bending and the maximum ranges of arm curvature theoretically achievable. Since one of our main goals was to determine the extent to which different ossicle types contributed to limiting the maximum bending curvature, we explored the skeletal kinematics for three conditions: the full skeletal
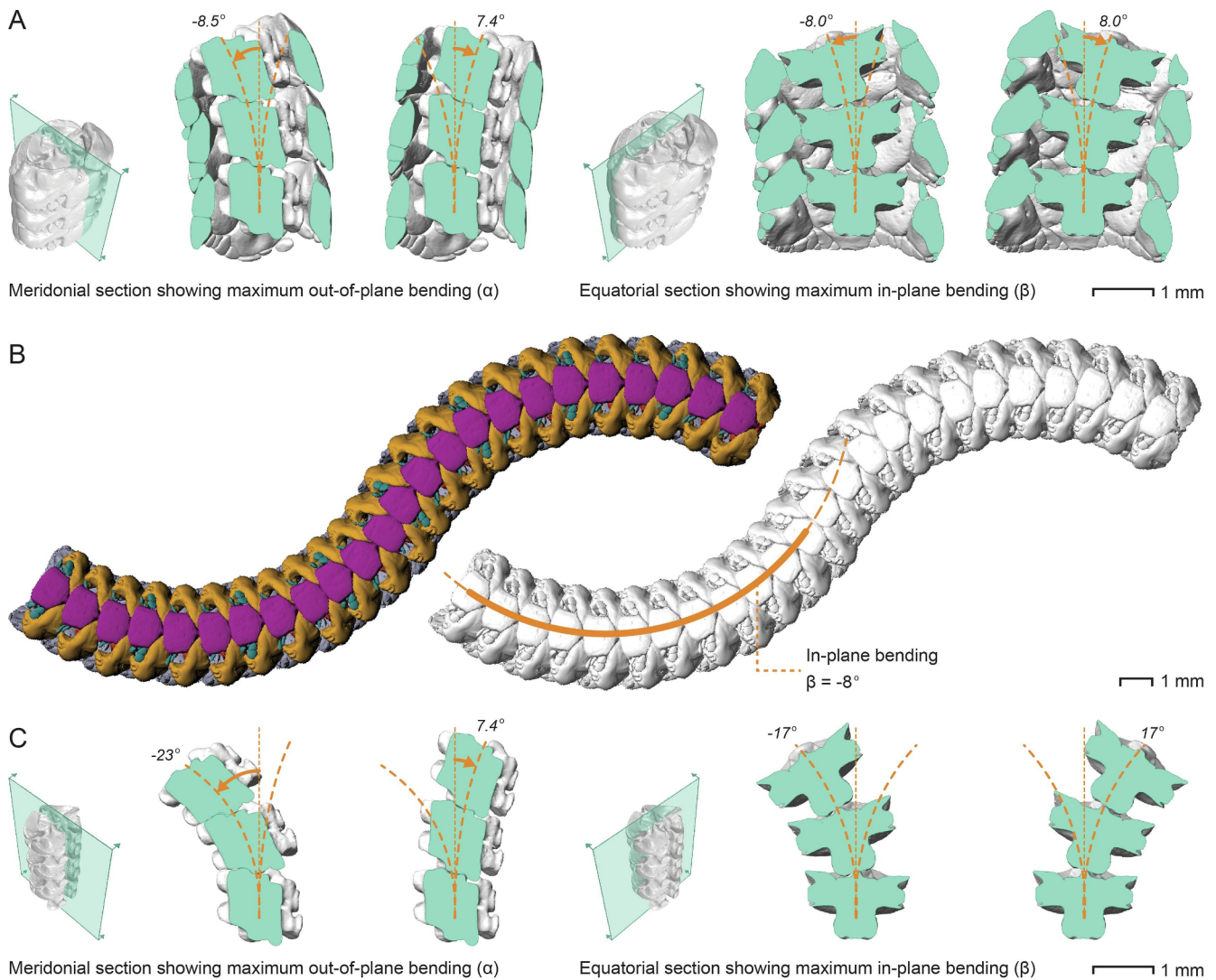
**Fig. 11.** Parametric models illustrating the bending curvatures of *O. esmarki* arms. A. For both in-plane (right) and out-of-plane bending (left), the maximum bending curvature is not affected by the presence of the small spines. B. By increasing the number of consecutive ossicle groups, we can reconstruct large scale sinusoidal arm motions and calculate their maximum achievable in-plane bending curvature. C. The parametric model consisting of only articulating vertebral ossicles demonstrates that the vertebral ossicle's morphology allows for greater bending curvatures (than is shown in A and B), both in-plane and out-of-plane, and as such, the maximum ranges of curvature achieved by arms of O. esmarki are brought about by the interplay of the entire assemblage of vertebral, crescent-shaped, and aboral ossicles.

system with spines, ossicle groups without spines, and vertebral ossicle articulation only.

Maximum in-plane bending angles between adjacent ossicle groups frequently observed during behavioral studies were quite similar between the three species, at 8.0, 9.5, and 13 degrees for *O. esmarki*, *O. papillosa* and *O. spiculata* respectively (Fig. 10A). However, due to differences in the relative thickness of the ossicle groups (being the greatest in *O. esmarki*), the resulting large-scale radius of curvature of the arms differed between species. These measured bending angles provided the input for our parametric models of the complete skeletal systems. In addition to the basic motions of the vertebral ossicles and other adjacent ossicles, the articulated spines also influenced large-scale ranges of motion. For example, long spines coming in contact with one another limit the arm's range of in-plane movement and specifically, the thicker, highly parallel spines found in *O. papillosa* hinder movement more than the thinner, more randomly organized spines of *O. spiculata*. As can be seen in both the live animals and the spine-containing models for *O. papillosa* and *O. spiculata*, the lateral flanges of the crescent-shaped ossicles do not come into contact with one another at

maximum bend (Fig. 10B, 12A, and 13A). The small spines of *O. esmarki*, in contrast, do not influence the maximum curvature (Fig. 10B and 11A). Animations generated from the parametric script illustrate the movable spines sliding past each other during in-plane bending (Video 1), while the arm spines do not play a role in limiting out-of-plane bending.

By removing the spines from the models, the range of in-plane motion significantly increased for the spiny brittle star species, up to 20 and 16 degrees for *O. papillosa* and *O. spiculata* respectively, since the large gaps between adjacent crescent-shaped ossicles in these two species allowed for a considerably greater amount of in-plane bending in the spine-free models (Video 2). In all three species, the in-plane bending motion in the spine-free models was now structurally limited by the crescent-shaped ossicles, with jamming of the crescent-shaped ossicles preventing over-rotation of the vertebral ossicles, when the arms were at maximum bend (Fig. 11A, 12B and 13B). These theoretical models therefore clearly demonstrated the roles of spines (in *O. papillosa* and *O. spiculata*) in limiting maximum arm bending curvatures, and thus provided an explanation for the higher ranges of curvature
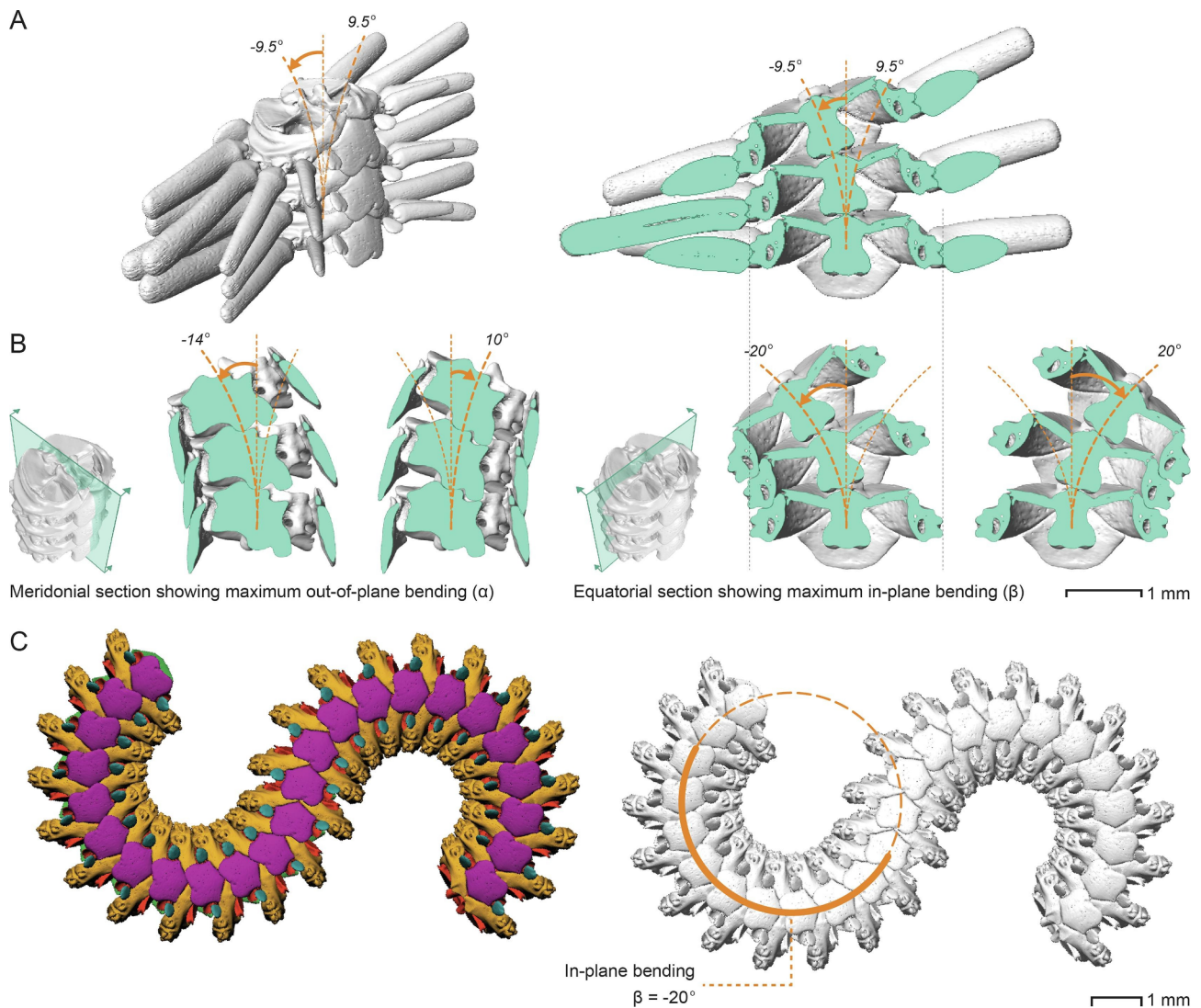
**Fig. 12.** Parametric models illustrating the bending curvatures of *O. papillosa* arms. A. In-plane movement is limited by the presence of spines, and as such, the crescent-shaped ossicles do not reach their point of collision. B. Without spines, however, the model shows that maximum in-plane bending curvature (right) increases, with the lateral flanges of the crescent-shaped ossicles jamming to prevent further motion, while the maximum out-of-plane bending curvature (left) remains unchanged. C. By increasing the number of consecutive ossicle groups, we can reconstruct large scale sinusoidal arm motions.

observed at the arm tips, which likely result from the presence of disproportionately fewer and smaller spines (Section 3.2).

During out-of-plane bending of the arms, mobile oral and aboral arm plates slide over the adjacent plates forming a high surface area shield that severely limits flexion. Section view animations clearly show how each plate's top and bottom morphology matches geometrically and allows for smooth sliding movements, while maintaining a high surface area contact (Video 3). While for *O. papillosa* and *O. spiculata* the large ranges of motion can be easily achieved due to the presence of large gaps between the adjacent crescent-shaped ossicles, the high number of articulation points within the fractal-like organization of compact aboral ossicles in *O. esmarki* can also easily accommodate both in-plane and out-of-plane movement (Video 4) (Fig. 11A).

The parametric model of *O. esmarki* consisting of only articulating vertebral ossicles shows that the vertebral ossicle's morphology allows for greater bending curvatures, up to 23 and 17 degrees for out-of-plane and in-plane bending respectively, demonstrating that the maximum ranges of curvature achieved by the arms of *O. esmarki* are brought about by the interplay of the entire ossicle assemblage (Fig. 11CD).

Using our parametric approach, we can also generate arms of any length by increasing the number of consecutive ossicle groups, revealing the minimum number required for sinusoidal motions (Video 5) (Fig. 11B, 12C, and 13C). By combining the models for both in-plane and out-of-plane bending, we can mimic the arm's full range of motion (Video 6).

### 3.4. Ossicle-ossicle contact zones and stereom microstructural features

With the insights obtained from the kinematic studies described above, we now had a relatively complete understanding of brittle star skeletal mobility and a starting point to begin investigating the functional roles of the ossicle-specific porosity gradients. The ossicles of ophiuroids, as well as those from other echinoderms, exhibit a robust three-dimensional porous architecture (the stereom) (Byrne, 1994; Czarkwiani et al., 2016). Differences in stereom porosity have been linked to regions where muscles and ligaments are attached (Bray, 1985; Macurda, 1976) and, at a smaller scale, identified as ring-like growth-bands of alternating density that are thought to reflect seasonal
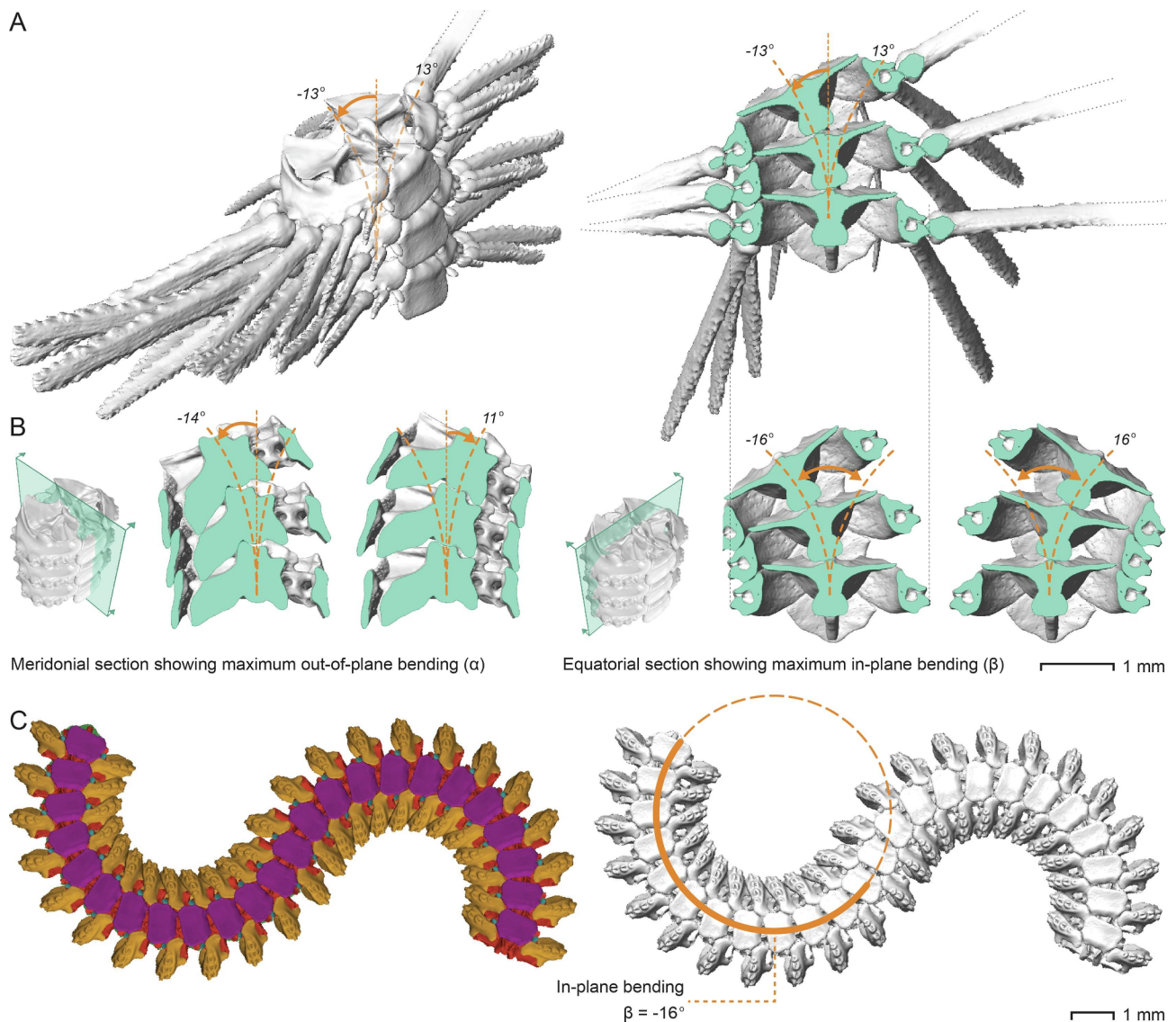
**Fig. 13.** Parametric models illustrating the bending curvatures of *O. spiculata* arms. A. In-plane movement is limited by the presence of spines, and as such, the crescent-shaped ossicles do not reach their point of collision. B. Without spines, however, the model shows that maximum in-plane bending curvature (right) increases, with the lateral flanges of the crescent-shaped ossicles jamming to prevent further motion, while the maximum out-of-plane bending curvature (left) remains unchanged. C. By increasing the number of consecutive ossicle groups, we can reconstruct large scale sinusoidal arm motions.

variations in growth rate (Byrne, 1994; Dahm and Brey, 1998; Gage, 1990; Quiroga and Sellanes, 2009).

Previous observations of low-porosity stereom had been interpreted as likely points of contact between adjacent ossicles, and thus acting as load-bearing surfaces designed to resist abrasion and redistribute applied stresses (Bray, 1985; LeClair, 1995). Based on our study's insights into arm kinematics, we subsequently set out to investigate the potential relationship between porosity gradients and the locations of ossicle-ossicle contact during arm bending.

With the ossicles functioning as an integrated jammable system to prevent over-motion of the arms, we were able to map out their areas of physical contact based on our parametric models. Points of contact include the nodes and sockets of complementary proximal and distal faces of the vertebral ossicles, the lateral flanges of the crescent-shaped ossicles as a result of maximum in-plane bending, and locations of interaction between (ab)oral plates and (ab)oral surfaces of the crescent-shaped ossicles (Fig. 14A) (Video 6).

Our scanning electron microscopy (SEM) analyses of vertebral and crescent-shaped ossicles of *O. papillosa* confirmed that areas of contact correspond with higher density stereom (Fig. 14B), and are consistent

with previous reports describing the smooth articular surfaces in vertebral ossicles (Bray, 1985; Byrne, 1994). Our SEM imaging studies also revealed that areas on the proximal and distal faces of the vertebral ossicles previously identified to bind muscular and connective tissues (Bray, 1985; Byrne, 1994; LeClair, 1996) correspond with small-pore and large-pore stereom, respectively. In addition, the locations of patches with roughened features described by LeClair (1995), and interpreted to relate to regions of surface wear, bear a striking similarity with the contact zones identified from our parametric models.

High resolution micro-CT scanning of a single vertebral ossicle also allowed us to obtain a quantitative three-dimensional model of its interior. The data revealed the presence of diverse microstructural stereom features as identified by Smith (1980) and previously recorded in ophiuroid vertebrae (Smith, 1990), including labyrinthine, galleried, and retiform geometries. In addition to the identification of specific geometric features, the 3D model also revealed pronounced variation in sub-surface stereom strut thicknesses (Fig. 15A) (Video 6), raising intriguing questions as to the potential roles of these complex internal gradients in dissipating applied loads.

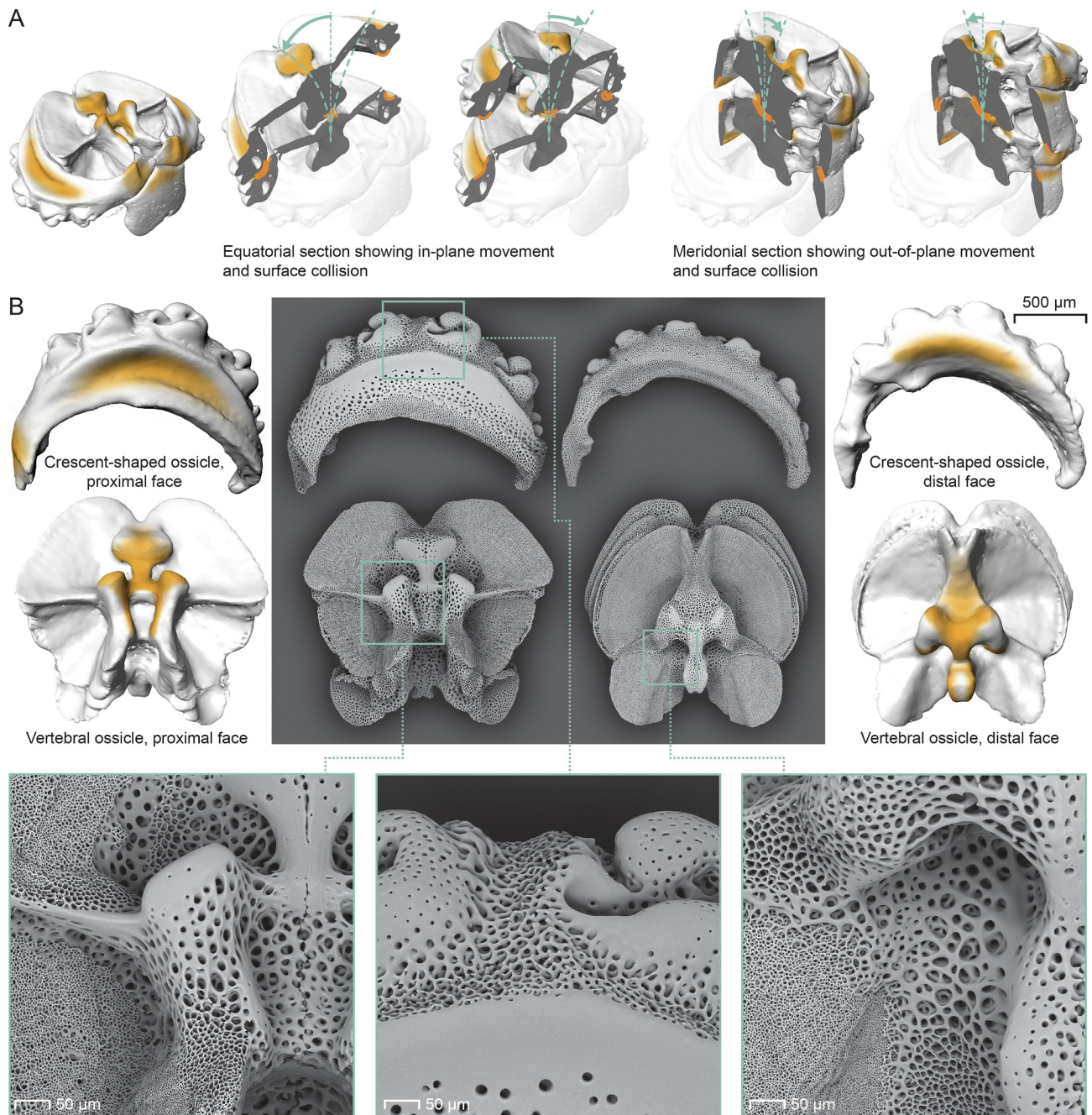In order to address these questions, the micro-CT data was

**Fig. 14.** Correlating collisional contact points between adjacent ossicles and microscale porosity gradients. A. Areas of physical contact (highlighted in orange) between ossicles during arm bending in *O. papillosa* identified from our parametric modeling motion studies. B. 3D surface geometries with areas of articulation in the crescent-shaped and vertebral ossicles juxtaposed to SEM images showing their porous structures confirm a correlation between areas of contact and high density (reduced porosity) stereom. Higher magnification views of the surface structures reveal complex porosity gradients moving from imperforate, to coarse, and fine stereom. (For interpretation of the references to color in this figure legend, the reader is referred to the web version of this article.)

quantitatively analyzed with respect to stereom microstructure. Because average porosity mapping values throughout the ossicle can potentially be misleading due to abrupt changes in local porosity within a sampled volume, which gives rise to average rather than site-specific and localized porosity values, the micro-CT data were analyzed instead with respect to strut thickness. Because of the methods by which the data were analyzed, however, mapping results illustrating strut thickness data do not necessarily correlate with visible variability in surface pore fraction as identified by SEM or from micro-CT surface reconstructions. Despite these differences, the analysis successfully identified significant differences in strut thickness throughout the vertebral ossicle as well as at specific locations previously identified as

areas of direct ossicle-ossicle contact (Fig. 15B), leading us to speculate that these microstructures play a role in large scale load transmission through the ossicle structure.

To confirm our suspicions regarding a correlation between strut thickness and local ossicle loading regimes, we performed a Finite Element Analysis on a chain of vertebral ossicles (Fig. 15C). Superimposition of the FE data on the 3D model of the high-resolution vertebral ossicle (Fig. 15DE) and SEM images of surface structures (Fig. 15F) shows that thicker struts correspond to regions of high tension or compression, while the predominantly low stress regions correspond to regions with low strut thickness.
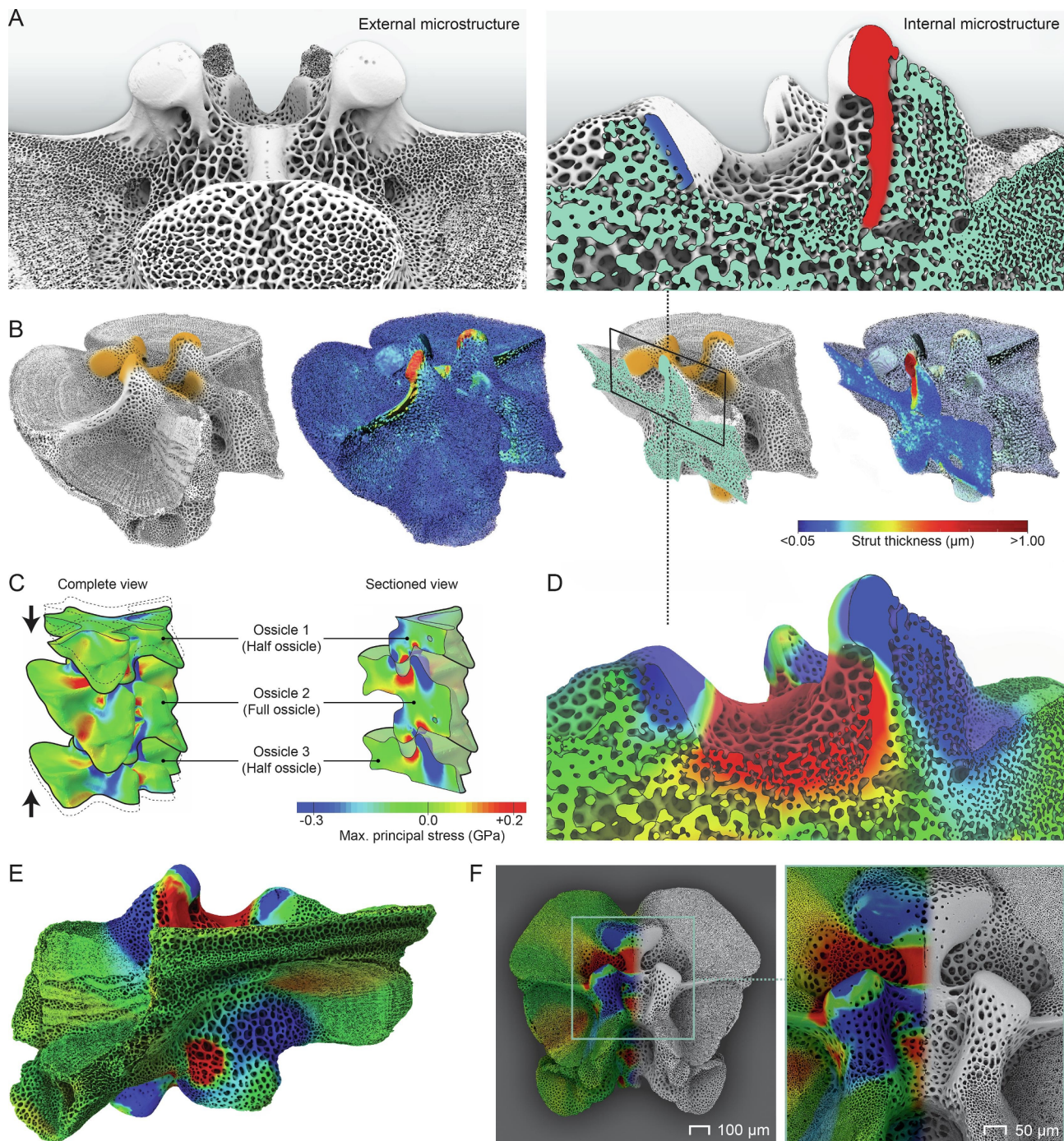
**Fig. 15.** Quantitative 3D mapping of *O. papillosa* ossicle microstructure. A. Left: proximal surface of a vertebral ossicle, viewed towards the oral side, clearly demonstrating the porosity gradients as well as gradients in void dimensions and strut width. Right: section plane (light green) matching the vertebral ossicle shown below in B, demonstrating high density/imperforate structural features that extend into the ossicle interior (red) versus those that remain superficial (blue). B. Surface (two left images) and sectioned (two right images) models correlating sites of ossicle collisional contact based on our parametric animations (grayscale images with orange highlights), with direct color-coded measurements of strut thickness based on high-resolution CT data. In the color scheme used in volume thickness mapping, blue corresponds to the minimum strut diameter and red corresponds to the largest. C. Finite Element model of a vertebral ossicle chain (left), including a solid geometry of one full vertebral ossicle (center) and two half ossicles adjacent to it. The simulation loaded the ossicle group in compression (denoted by the black arrows) and the resulting stress distribution maps were generated. Negative and positive values and their associated colors represent areas of compression and tension, respectively. Using the same color scale for C-F, these results demonstrate a clear link between local compressive or tensile loading and the presence of thicker, higher density struts in both sectioned (D) and complete ossicle reconstructions (E). F. The FE model superimposed upon SEM images of the proximal face of a vertebral ossicle (cf. Fig. 14B) shows that areas with thicker struts correspond to regions of high tension (red) or compression (blue), while the predominantly low stress regions (green) correspond to regions of low strut thickness. (For interpretation of the references to color in this figure legend, the reader is referred to the web version of this article.)

## 4. Discussion

As demonstrated in the present study, arm motion in brittle stars results from the coordinated interaction of hundreds of individual skeletal elements that are organized into serially repetitive multi-ossicle units. Despite the fact that skeletal architecture varies widely across different brittle star families and species (Lyman,1882), and while additional studies are still needed to fully validate the suitability of these modeling approaches across the Ophiuroidea (Clark et al., 2019), the integrated workflow reported here provides a robust framework for performing multi-scale skeletal kinematic investigations in this highly mobile group of echinoderms.

For example, at the single ossicle level, our finite element, scanning electron microscopy, and high resolution micro-CT results reveal that micro-structural gradients in ossicle strut thickness are closely correlated with their specific functional roles, as demonstrated through (1) an increase in stereom surface area for muscle and soft tissue attachment, (2) an increase in strut relative thickness in regions of tensile or compressive loading, and (3) an increase in skeletal mass to minimize abrasion during repetitive ossicle-ossicle contact events.

At the scale of multiple ossicles, our interdisciplinary approach provides a roadmap for exploring other aspects of ophiuroid anatomy and ecology. For example, the parametric nature of our modeling workflow permits precise modifications to ossicle sizes, thus allowing direct investigations into the roles of arm taper angle and arm tip geometries on grasping and food capture (Austin and Hadfield, 1980).

At the whole animal level, since the global and local motions of the arms are both independently addressable and customizable, our workflow permits the tiling of multiple skeletal units in order to model large-scale sinusoidal motions, as shown in Figs. 11–13. These capabilities thus provide an important stepping stone toward the development of realistic, whole-animal gait simulations for investigating habitat-specific navigation across structurally complex substrates (Astley, 2012; Kano et al., 2019). Beyond the study of adult brittle stars, our approach could also be used to model changes in gait geometry and ranges of motion in post-larval specimens resulting from age-related modifications to ossicle ornamentations (Martynov et al., 2015).

From a biodiversity and evolutionary perspective, these techniques can be expanded to investigate and reconstruct the ranges of motion in precious preserved museum and fossil specimens of both modern and extinct brittle star species (O'Hara et al., 2014). These tools could also be applied to the study of other ophiuroids such as basket stars, or other echinoderms with serially repetitive skeletal systems such as the crinoids. Additionally, by incorporating muscular and connective tissue 3D structure data (Arnold et al., 2014), our approach could further be adapted to study ranges of motion in other (non-echinoderm) kinematic axial skeletal systems, and as such, could be useful in elucidating ranges of motion in snakes (Xing et al., 2018), fish (Jayne and Lauder, 1995; Nowroozi and Brainerd, 2013), sauropod dinosaur necks (Cobley et al., 2013), or for investigating adaptations in spinal flexibility during the early evolution of terrestrial tetrapods (Pierce et al., 2013).

While the direct inputs for the construction of our arm kinematic models were provided from the segmentation of micro-CT data, future iterations of our workflow to produce fully tunable parametric ossicle networks could instead rely solely on the input of geometric landmarks (Connors et al., 2019). Further refinement of these models could also be achieved through the incorporation of data derived from *in situ* digital videofluoroscopic or synchrotron-based imaging during live animal locomotory studies (Zheng et al., 2003; Clark et al., 2019), thus significantly expanding the utility of these approaches for implementation in patient-specific biomedical or veterinary contexts (Gurley et al., 2009; MacIntyre et al., 2006; Van Sint Jan et al., 2002).

## Declaration of Competing Interest

The authors declare that they have no known competing financial interests or personal relationships that could have appeared to influence the work reported in this paper.

## Author contributions

JCW supervised the research. LT developed the 3D parametric modeling and animation tools and analyzed the data; LJF and JCW performed the live animal behavioral and photographic studies; LT, DB, and JCW performed the micro-CT measurements; MCF, LT, and JCW designed, performed, and analyzed the finite element data; CP collected and maintained the research specimens; RJW and JCW secured funding for the research; LT and JCW wrote the original manuscript draft with subsequent edits from the rest of the co-authors.

## Appendix A. Supplementary data

Supplementary data to this article can be found online at https://doi.org/10.1016/j.jsb.2020.107481.

## References

Arnold, P., Fischer, M.S., Nyakatura, J.A., 2014. Soft tissue influence on ex vivo mobility in the hip of Iguana: comparison with in vivo movement and its bearing on joint motion of fossil sprawling tetrapods. J. Anat. 225, 31–41. https://doi.org/10.1111/joa.12187.

Arshavskii, Y.I., Kashin, S.M., Litvinova, N.M., Oriovskii, G.N., Feldman, A.G., 1976. Types of locomotion in ophiurans. Neurophysiology 8, 398–404. https://doi.org/10.1007/BF01063602.

Arshavskii, Y.I., Kashin, S.M., Litvinova, N.M., Orlovskii, G.N., Feldman, A.G., 1975. Coordination of arm movement during locomotion in Ophiurans 8, 404–410. doi: 10.1007/BF01063603.

Astley, H.C., 2012. Getting around when you're round: quantitative analysis of the locomotion of the blunt-spined brittle star. Ophiocoma echinata 215, 1923–1929. https://doi.org/10.1242/jeb.068460.

Austin, W.C., Hadfield, M.G., 1980. Ophiuroidea: the brittle stars. In: Morris, R.H., Abbott, D.P., Haderlie, E.C. (Eds.), Intertidal Invertebrates of California. Stanford University Press, Stanford, California.

Barnes, R.D., 1987. Invertebrate Zoology, 5th ed. Saunders College Pub.

Bray, R.D., 1985. Stereom microstructure of the vertebral ossicles of the Caribbean ophiuroid Ophiocoma echinata. In: Harmelin Vivien, M., Salvat, B. (Eds.), Proceedings of the Fifth International Coral Reef Congress, Tahiti. pp. 279–284.

Byrne, M., 1994. Ophiuroidea. In: Harrison, F.W., Woollacott, R.M. (Eds.), Microscopic Anatomy of Invertebrates. AR Liss, New York, pp. 247–343.

Byrne, M., Hendler, G., 1988. Arm structures of the ophiomyxid brittlestars (Echinodermata: Ophiuroidea: Ophiomyxidae), in: Burke (Ed.), Echinoderm Biology. Balkema, Rotterdam, pp. 687–695.

Carnevali, M.D.C., 2006. Regeneration in echinoderms: repair, regrowth, cloning. Invertebrate Survival J. 3, 64–76.

Clark, E.G., Hutchinson, J.R., Darroch, S.A.F., Mongiardino Koch, N., Brady, T.R., Smith, S.A., Briggs, D.E.G., 2018. Integrating morphology and in vivo skeletal mobility with digital models to infer function in brittle star arms. J. Anat. 233, 696–714. https://doi.org/10.1111/joa.12887.

Clark, E.G., Fezzaa, K., Burke, J.E., Racicot, R.A., Shaw, J.O., Westacott, S., Briggs, D.E.G., 2019. A farewell to arms: using X-ray synchrotron imaging to investigate autotomy in brittle stars. Zoomorphology 138 (3), 419–424. https://doi.org/10.1007/s00435-019-00451-7.

Cobb, J.L.S., Stubbs, T.R., 1981. The giant neurone system in ophiuroids I. The general morphology of the radial nerve cords and circumoral nerve ring. Cell Tissue Res. 2019, 197–207. https://doi.org/10.1007/BF00210028.

Cobley, M.J., Rayfield, E.J., Barrett, P.M., 2013. Inter-vertebral flexibility of the ostrich neck: implications for estimating sauropod neck flexibility. PLoS ONE 8 (8), e72187. https://doi.org/10.1371/journal.pone.0072187.

Connors, M., Yang, T., Hosny, A., Deng, Z., Yazdandoost, F., Massaadi, H., Eernisse, D., Mirzaeifar, R., Dean, M.N., Weaver, J.C., Ortiz, C., Li, L., 2019. Bioinspired design of flexible armor based on chiton scales. Nat. Commun. 10, 5413. https://doi.org/10.1038/s41467-019-13215-0.

Czarkwiani, A., Cinzia, F., Dylus, D.V., Sugni, M., Oliveri, P., 2016. Skeletal regeneration in the brittle star Amphiura filiformis. Front. Zool. 13. https://doi.org/10.1186/s12983-016-0149-x.

Czarkwiani, A., Dylus, D.V., Oliveri, P., 2013. Expression of skeletogenic genes during arm regeneration in the brittle star Amphiura filiformis. Gene Expr. Patterns 13, 464–472. https://doi.org/10.1016/j.gep.2013.09.002.

Dahm, C., Brey, T., 1998. Determination of growth and age of slow growing brittle stars (Echinodermata: Ophiuroidea) from natural growth bands 78, 941–951. doi: 10.1017/S0025315400044891.

Emson, R.H., Wilkie, I.C., 1982. The arm-coiling response of Amphipholis squamata (Delle Chiaje). In: International Echinoderms Conference, Tampa Bay. A.A. Balkema, Rotterdam.

Frølich, S., Weaver, J.C., Dean, M.N., Birkedal, H., 2017. Uncovering nature's design strategies through parametric modeling, multi-material 3D printing, and mechanical testing. Adv. Eng. Mater. 19 (6), 1600848. https://doi.org/10.1002/adem.201600848.

Gage, J.D., 1990. Skeletal growth markers in the deep-sea brittle stars Ophiura ljungmani and Ophiomusium lymani. Mar. Biol. 104, 427–435. https://doi.org/10.1007/BF01314346.

Glaser, O.C., 1907. Movement and problem solving in Ophiura brevispina. J. Exp. Zool. 4, 203–220. https://doi.org/10.1002/jez.1400040203.

Gurley, K.A., Chen, H., Guenther, C., Nguyen, E.T., Rountree, R.B., Schoor, M., Kingsley, D.M., 2009. Mineral formation in joints caused by complete or joint-specific loss of ANK function. J. Bone Miner. Res. 21, 1238–1247. https://doi.org/10.1359/jbmr.060515.

Hyman, L.H., 1940. Class Ophiuroidea, in: The Invertebrates. Volume 4 Echinodermata. pp. 589–688.

Hendler, G., Miller, J.E., 1984. Ophioderma devaneyi and Ophioderma ensiferum, new brittle star species from the western Atlantic (Echinodermata: Ophiuroidea). Proc. Biol. Soc. Wash. 97, 442–461.

Jayne, B.C., Lauder, G.V., 1995. Speed effects on midline kinematics during steady un-dulatory swimming of largemouth bass, Micropterus salmoides. J. Exp. Biol. 198, 585–602.

Kano, T., Sato, E., Ono, T., Aonuma, H., Matsuzaka, Y., Ishiguro, A., 2017. A brittle star-like robot capable of immediately adapting to unexpected physical damage. R. Soc. Open Sci. 4, 171200. https://doi.org/10.1098/rsos.171200.

Kano, T., Kanauchi, D., Ono, T., Aonuma, H., Ishiguro, A., 2019. Flexible coordination of flexible limbs: decentralized control scheme for inter- and intra-limb coordination in brittle stars' locomotion. Front. Neurorob. 13, 104. https://doi.org/10.3389/fnbot.2019.00104.

Lawrence, J., 1987. A Functional Biology of Echinoderms. The John Hopkins University Press, Baltimore.

LeClair, E.E., 1996. Arm joint articulations in the ophiuran brittlestars (Echinodermata: Ophiuroidea): a morphometric analysis of ontogenetic, serial, and interspecific variation. J. Zool. 240, 245–275. https://doi.org/10.1111/j.1469-7998.1996.tb05283.x.

LeClair, E.E., 1995. Microstructural roughness of skeletal calcite in ophiuroid vertebral ossicles: evidence of wear? Tissue Cell 27, 539–543. https://doi.org/10.1016/S0040-8166(05)80062-X.

LeClair, E., LaBarbara, M.C., 1997. An in vivo comparative study of intersegmental flexibility in the ophiuroid arm. Biol. Bull. 193, 77–89. https://doi.org/10.2307/1542737.

Litvinova, N.M., 1994. The life forms of ophiuroidea (based on the morphological structures of their arms). In: Echinoderms through Time: Proceedings on the Eighth International Echinoderm Conference, Dijon, France, 5-10 September, 1993. Balkema, Rotterdam, pp. 449–454.

Lyman, T., 1882. Report on the Ophiuroidea dredged by H.M.S. Challenger during the years 1873–1876. Reports of Science Research Voyage of H.M.S. Challenger. Zoology 5, 1–386.

MacIntyre, N.J., Hill, N.A., Fellows, R.A., Ellis, R.E., Wilson, D.R., 2006. Patellofemoral joint kinematics in individuals with and without patellofemoral pain syndrome. J. Bone Joint Surg. 88 (12), 2596–2605. https://doi.org/10.2106/JBJS.E.00674.

Macurda, D.B., 1976. Skeletal modifications related to food capture and feeding behavior of the basketstar Astrophyton. Paleobiology 2, 1–7. https://doi.org/10.1017/S0094837300003262.

Martynov, A., Ishida, Y., Irimura, S., Tajiri, R., O'Hara, T., Fujita, T., 2015. When onto-geny matters: a new Japanese species of brittle star illustrates the importance of considering both adult and juvenile characters in taxonomic practice. PLoS ONE 10, e0139463. https://doi.org/10.1371/journal.pone.0139463.

Meglitsch, P.A., Schram, F.R., 1991. Echinodermata. In: Invertebrate Zoology. pp. 523–564.

Moore, A., Cobb, J.L.S., 1986. Neurophysiological studies on the detection of mechanical stimuli by Ophiura ophiura. J. Exp. Mar. Biol. Ecol. 104, 125–141. https://doi.org/10.1016/0022-0981(86)90100-0.

Mosher, C.V., Watling, L., 2009. Partners for life: a brittle star and its octocoral host. Mar. Ecol. Prog. Ser. 397, 81–88. https://doi.org/10.3354/meps08113.

Nowroozi, B.N., Brainerd, E.L., 2013. X-ray motion analysis of the vertebral column during the startle response in striped bass, Morone saxatilis. J. Exp. Biol. 216, 2833–2842. https://doi.org/10.1242/jeb.085118.

O'Hara, T.D., Hugall, A.F., Thuy, B., Moussalli, A., 2014. Phylogenomic resolution of the class ophiuroidea unlocks a global microfossil record. Curr. Biol. 24, 1874–1879. https://doi.org/10.1016/j.cub.2014.06.060.

Otsu, N., 1979. A threshold selection method from gray-level histograms. IEEE Trans. Systems Man Cybernetics 9 (1), 62–66. https://doi.org/10.1109/TSMC.1979.4310076.

Pentreath, R.J., 1970. Feeding mechanisms and the functional morphology of podia and spines in some New Zealand ophiuroids (Echinodermata). J. Zool. 161, 395–429. https://doi.org/10.1111/j.1469-7998.1970.tb04520.x.

Pierce, S.E., Ahlberg, P.E., Hutchinson, John R., Molnar, J.L., Sanchez, S., Tafforeau, P., Clack, J.A., 2013. Vertebral architecture in the earliest stem tetrapods. Nature 494 (7436), 226–229. https://doi.org/10.1038/nature11825.

Quiroga, E., Sellanes, J., 2009. Growth and size-structure of Stegophiura sp. (Echinodermata: Ophiuroidea) on the continental slope off central Chile: a comparison between cold seep and non-seep sites. J. Mar. Biol. Assoc. United Kingdom 89, 421–428. https://doi.org/10.1017/S0025315408002786.

Romanes, G.J., 1893. Jelly-fish, star-fish, and sea-urchins. Being a research on primitive nervous systems. International scientific series, New York, NY.

Saita, A., Carnevali, M.D.C., Canonaco, M., 1982. Muscle system organization in the echinoderms. I. Intervertebral muscles of Ophioderma longicaudum (Ophiuroidea). J. Submicroscopic Cytol. 14, 291–304.

Skold, M., Rosenberg, R., 1996. Arm regeneration frequency in eight species of ophiur-oidea (Echinodermata) from European sea areas. J. Sea Res. 35, 353–362. https://doi.org/10.1016/S1385-1101(96)90762-5.

Sloan, N.A., Campbell, A.C., 1982. Perception of food, in: Jangoux, M., Lawrence, J.M. (Eds.), Echinoderm Nutrition. A.A. Balkema, Rotterdam, pp. 1–23.

Smith, A.B., 1980. Stereom microstructure of the echinoid test. Special Papers in Paleontology 25, 1-81.

Smith, A.B., 1990. Biomineralization in Echinoderms. In: Carter, J.G. (Ed.), Skeletal biomineralization: patterns, processes and evolutionary trends. Volume 1. New York: Van Nostrand Reinhold, pp. 413–443.

Smith, A.B., Paterson, G.L.J., Lafay, B., 1995. Ophiuroid phylogeny and higher taxonomy: morphological, molecular and palaeontological perspectives. Zool. J. Linn. Soc. 114, 213–243. https://doi.org/10.1006/zjls.1995.0024.

Smith, J.E., 1965. Echinodermata. In: Bullock, T.H., Horridge, G.A. (Eds.), Structure and Function in the Nervous Systems of Invertebrates. W. H. Freeman, San Francisco, pp. 1519–1558.

Stauber, M., Märkel, K., 1988. Comparative morphology of muscle-skeleton attachments in the Echinodermata. Zoomorphology 108, 137–148. https://doi.org/10.1007/BF00363930.

Stöhr, S., O'Hara, T., Thuy, B. (Eds.), 2018. World Ophiuroidea database.

Stöhr, S., O'Hara, T., Thuy, B., 2012. Global diversity of brittle stars (Echinodermata: Ophiuroidea). PLoS ONE 7. https://doi.org/10.1371/journal.pone.0031940.

Thuy, B., Stöhr, S., 2011. Lateral arm plate morphology in brittle stars (Echinodermata: Ophiuroidea): new perspectives for ophiuroid micropalaeontology and classification. Zootaxa 3013, 1–47. https://doi.org/10.11646/zootaxa.3013.1.1.

Van Sint Jan, S., Salvia, P., Hilal, I., Sholukha, V., Rooze, M., Clapworthy, G., 2002. Registration of 6-DOFs electrogoniometry and CT medical imaging for 3D joint modeling. J. Biomech. 35 (11), 1475–1484. https://doi.org/10.1016/S0021-9290(02)00074-X.

Warner, G., 1982. Food and feeding mechanisms: Ophiuroidea, in: Jangoux, M., Lawrence, J.M. (Eds.), Echinoderm Nutrition. A.A. Balkema, Rotterdam, pp. 161–184.

Warner, G.F., Woodley, J.D., 1975. Suspension-feeding in the brittle-star Ophiothrix fragilis. J. Marine Biol. Assoc. United Kingdom 55, 199–210. https://doi.org/10.1017/S0025315400015848.

Watanabe, W., Kano, T., Suzuki, S., Ishiguro, A., 2012. A decentralized control scheme for orchestrating versatile arm movements in ophiuroid omnidirectional locomotion. J. R. Soc. Interface 7, 102–109. https://doi.org/10.1098/rsif.2011.0317.

Wilkie, I.C., 1978. Arm autotomy in brittlestars (Echinodermata: Ophiuroidea). J. Zool. 186, 311–330.

Wilkie, I.C., 2016. Functional morphology of the arm spine joint and adjacent structures

of the brittlestar Ophiocomina nigra (Echinodermata: Ophiuroidea). PLoS ONE 11 (12), e0167533. https://doi.org/10.1371/journal.pone.0167533.

Wood, J.G., 1898. Animate Creation. Selmar Hess, New York.

Xing, L., Caldwell, M.W., Chen, R., Nydam, R.L., Palci, A., Simões, T.R., McKellar, R.C., Lee, M.S.Y., Liu, Y., Shi, H., Wang, K., Bai, M., 2018. A mid-Cretaceous embryonic-to-neonate snake in amber from Myanmar. Sci. Adv. 4 (7), eaat5042. https://doi.org/10.1126/sciadv.aat5042.

Zeleny, C., 1903. A study of the rate of regeneration of the arms in the brittle-star. Ophioglypha lacertosa 6, 12–17. https://doi.org/10.2307/1535809.

Zheng, Y., Nixon, M.S., Allen, R., 2003. Lumbar spine visualisation based on kinematic analysis from videofluoroscopic imaging. Med. Eng. Phys. 25 (3), 171–179. https://doi.org/10.1016/S1350-4533(02)00182-0.